Dynamics of the Great Oxidation Event from a 3D photochemical-climate model

Adam Yassin Jaziri[1], Benjamin Charnay[2], Franck Selsis[1], Jérémy Leconte[1], and Franck Lefèvre[3]

[1]Laboratoire d'astrophysique de Bordeaux, Univ. Bordeaux, CNRS, B18N, allée Geoffroy Saint-Hilaire, 33615 Pessac, France

[2]LESIA, Observatoire de Paris, Université PSL, CNRS, Sorbonne Université, Université de Paris, 5 place Jules Janssen, 92195 Meudon, France.

[3]Laboratoire Atmosphères, Milieux, Observations Spatiales (LATMOS), CNRS/IPSL/UPMC, Paris, France.

Correspondence: Adam Yassin Jaziri (adam.jaziri@u-bordeaux.fr)

Abstract. From the Archean toward the Proterozoic, the Earth's atmosphere underwent a major shift from anoxic to oxic conditions, around 2.4 to 2.1 Gyr, known as the Great Oxidation Event (GOE). This rapid transition may be related to an atmospheric instability caused by the formation of the ozone layer. Previous works were all based on 1D photochemical models. Here, we revisit the GOE with a 3D photochemical-climate model to investigate the possible impact of the atmospheric circulation and the coupling between the climate and the dynamics of the oxidation. We show that the diurnal, seasonal and transport variations do not bring significant changes compared to 1D models. Nevertheless, we highlight a temperature dependence for atmospheric photochemical losses. A cooling during the late Archean could then have favored the triggering of the oxygenation. In addition, we show that the Huronian glaciations, which took place during the GOE, could have introduced a fluctuation in the evolution of the oxygen level. Finally, we show that the oxygen overshoot which is expected to have occurred just after the GOE, was likely accompanied by a methane overshoot. Such high methane concentrations could have had climatic consequences and could have played a role in the dynamics of the Huronian glaciations.

1 Introduction

The oldest rocks found today in the northwestern Canada date to 4.00-4.03 Gyr ago (Bowring and Williams, 1999). The stromatolites from the Barberton formation of South Africa and the Warrawoona formation of Australia dated to about 3.5 Gyr ago are accepted as a sign of life (Furnes et al., 2004; Awramik et al., 1983; Brasier et al., 2006). The microbial fossils dated to 2.6 Gyr ago found in the Campbell formation of Cape Province in South Africa are identifiable as cyanobacteria (Pierrehumbert, 2010) as many other evidences starting 2.8 Gyr ago (Nisbet et al., 2007; Crowe et al., 2013; Lyons et al., 2014; Planavsky et al., 2014; Satkoski et al., 2015; Schirrmeister et al., 2016). Cyanobacteria are known to produce oxygen by photosynthesis. Oxygenic photosynthesis was likely already developed before the Great Oxidation Event (GOE) that happened around 2.4 to 2.1 Gyr ago. During this event, the amount of oxygen increased from less than 10^{-5} present atmospheric level (PAL) to a maximum of 10^{-1} PAL around 2.2 Gyr ago before fluctuating approximately between 0.4 and 10^{-4} PAL (Lyons et al., 2014).

The best constraints on the GOE come from sulfur isotopic ratios in precambrian rocks (Farquhar et al., 2007; Lyons et al., 2014). In the Archean anoxic atmosphere, the sulfur photochemistry was responsible for mass-independent fractionation of sulphur isotopes in sedimentary rocks (Kasting et al., 1989; Pavlov and Kasting, 2002).

The loss of mass-independent fractionation in sedimentary rocks less than 2.5 Gyr ago is explained by a modification of sulfur photochemistry main pathways due to the rise of the amount of oxygen, starting from 10^{-5} present atmospheric level (PAL) (Pavlov and Kasting, 2002). This is directly linked to the amount of UV flux received for the sulfur photochemistry, which could be reduced by the appearance of ozone at higher oxygen level (Zahnle et al., 2006).

The GOE represents a major event in the history of the Earth. It profoundly impacted the atmospheric and oceanic chemistry, the climate, the mineralogy and the evolution of life. O_2 was a poison for a lot of anoxygenic form of life supposed already developed. Consequently, the GOE likely induced a retreat for anoxygenic form of life, including heterotrophic methanogens (i.e. organisms producing methane). Methane may have been more abundant in the anoxic Archean atmosphere than today (1.8 ppm), with levels as high as 10^4 pmm according to Catling and Zahnle (2020). Such high methane concentrations would have produced a significant greenhouse effect. A variation of 10 times the abundance of methane changes the mean surface temperature of about 4 K according to Charnay et al. (2020). Furthermore, Sauterey et al. (2020) show that the diminution of CH4 combined with the regulation of CO2 by the carbonate-silicate cycle favors the triggering of an ice age. The decrease of the biological methane productivity and the methane photochemical lifetime could have reduced its abundance and thus its warming contribution, potentially triggering the Huronian glaciations that took place between 2.4 and 2.1 Gyr (Kasting et al., 1983; Haqq-Misra et al., 2008) The GOE is a key event to understand the co-evolution of life and environment on Earth but also on exoplanets. However, major questions remain concerning the triggering and the dynamics of the GOE.

Before the appearance of oxygenic photosynthesis, the redox state of the atmosphere was ruled by the balance between reductant fluxes from volcanism and metamorphism and the hydrogen atmospheric escape (Catling et al., 2001). The appearance of oxygenic photosynthesis, which was much more efficient than previous metabolisms, relying on ubiquitous H_2O, CO_2 and light, profoundly changed the biogeochemical cycles. The oxygen is produced by oxygenic photosynthesis (summarized by formula (1)), which can be reversed by aerobic respiration.

$$CO_2 + H_2O + h\nu \longrightarrow CH_2O + O_2 \tag{1}$$
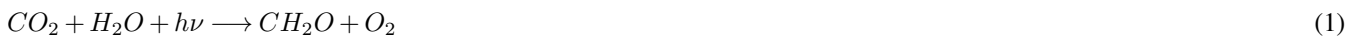
The burial of organic carbon (a very small fraction of the net primary productivity) allows the accumulation of oxygen until that an equilibrium is reached between the burial of organic carbon, the reductant fluxes, the oxidative weathering (i.e. the oxidation of buried organic carbon re-exposed to the surface by plate tectonics) and the hydrogen escape. Assuming a methane-rich atmosphere, atmospheric oxygen is also strongly coupled to methane through the reaction of methane oxidation:

$$CH_4 + 2O_2 \longrightarrow CO_2 + 2H_2O \tag{2}$$

On the early Earth and once oxygenic photosynthesis appeared, methane would have been mostly produced by the fermentation of organic matter followed by acetogenic methanogenesis:

$$2CH_2O \longrightarrow CH_3COOH \longrightarrow CH_4 + CO_2 \tag{3}$$

For aerobic conditions, it could have been consumed by oxygenic methanotrophy, similar to reaction (2). Goldblatt et al. (2006) and Claire et al. (2006) developed simplified models of the biogeochemical cycles of O_2 and CH_4. They proposed scenarios for the evolution of the amount of oxygen and methane and the dynamics of the GOE.

Several hypotheses have been proposed to explain the mechanisms and timing of the GOE. The hydrogen escape is one of them, proposed by Catling et al. (2001). Considering the irreversible oxidation of methane by the reaction (4) :

$$CH_4 + O_2 \longrightarrow CO_2 + 4H(\uparrow) \tag{4}$$
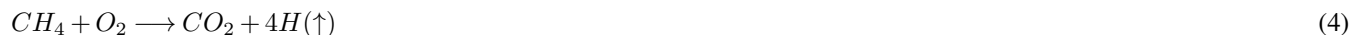
and the reverse reaction (2), we get a chain of reaction that causes a net gain of oxygen by transforming $2H_2O$ into O_2 (5) :

$$CO_2 + 2H_2O \longrightarrow CH_4 + 2O_2 \longrightarrow CO_2 + O_2 + 4H(\uparrow) \tag{5}$$

Emergence of continents and subaeriel volcanism is another hypothesis developed in Gaillard et al. (2011) that led to a change of the chemical composition and the oxidation state of sulfur volcanic gases, precipitating the atmospheric oxygenation.

But whatever precipitated the GOE, the rise of oxygen seems to be linked to an atmospheric instability caused by the formation of the ozone layer and its impact on the photochemical methane oxidation (Goldblatt et al., 2006). Slowly increasing O_2, by oxygenic photosynthesis, would have accumulate enough starting the ozone layer formation. The ozone layer provide a photochemical shield which limit the oxygen photochemical destruction leading to the methane oxidation. Therefor the oxygen could have accumulate more easily, producing more ozone, shielding more efficiently the oxygen destruction and then rising an instability of growing oxygen until others processes would have limited the oxygen abundance, such as rock oxidation.

In this paper we focus on the atmospheric photochemical losses by methane oxidation associated to the GOE. Previous 1D studies of Goldblatt et al. (2006); Claire et al. (2006); Zahnle et al. (2006), developed dynamical models of the GOE based on 1D photochemical models. In this study, we use for the first time a 3D Global Climate Model to compute the chemical lifetime of the different species and to explore 3D effects. Since the oxygen build-up is linked to the formation of the ozone, we could expect effects from the latitudinal/longitudinal ozone distribution or from the variations of UV irradiation by the seasonal and the diurnal cycles. We also investigate the potential links between the GOE and the Huronian glaciations. In particular, the consequences of a cold climate (.e.g. a snowball Earth event) on the photochemistry have never been studied.

Following, we describe the atmospheric model used for this study in Section 2. In Section 3, we analyze the photochemistry of the late Archean/Neoproterozoic with the 3D model, highlighting the chemical lifetimes and the impact of the global mean surface temperature. Based on these results, we describe the dynamical evolution of O_2 and CH_4 during the GOE in Section 4, highlighting consequences of the Huronian glaciations. We finish with a summary and perspectives in Sect. 5.

2 Model

A 3D photochemical global climate model is used to characterize photochemical oxygen losses in the atmosphere, dominated by methane oxidation in the model. The model, the LMD-generic, is a generic Global Climate Model (GCM) initially developed

at the Laboratoire de Météorologie Dynamique (LMD) for the study of a wide range of atmospheres. It allows to model easily different atmospheres, which makes it widely used, for instance to study early climates in the solar system (Forget et al., 2012; D. Wordsworth et al., 2012; Charnay et al., 2013; Turbet et al., 2020b) or extrasolar planets (Selsis et al., 2011; Leconte et al., 2013; Bolmont et al., 2016; Fauchez et al., 2019; Turbet et al., 2020a). From the photochemical module of the martian version of the model (Lefèvre et al., 2004), we have develop a generic version. It allows to easily adapt the chemical network and it introduces the calculation of the photolysis rates and their heating rates within the model.

The chemical network is derived from the REPROBUS model of the present Earth stratosphere (Lefèvre et al., 1998) but adapted to the assumed composition. Halogen, heterogeneous and nitrogen chemistry is not taken into account due to the weak constraints available. Furthermore, halogen and heterogeneous chemistry have a negligible effect on the oxygen chemistry studied. In contrast, the chemical network includes a detailed methane chemistry. It allows to take into account the different pathways of the methane oxidation balance. The methane network is built according to Arney et al. (2016) and Pavlov et al. (2001). The whole chemical network is detailed in appendix A.

We have developed a new photochemical module for the LMD-generic code. Although previous versions of the code already included photochemical processes, they were hard-coded to specific atmospheres. The module is now flexible and no longer uses pre-computed photolysis rates, which are now computed using the actual absorbers abundances in the model. The module also accounts for the heating rates by photolyses although the abundance of O_3 in the present study is too low to yield significant heating. Including the heating by photodissociations will nevertheless be essential for other potential applications of the generic model, including Earth-like oxygen-rich atmospheres.

The GCM is adapted to the supposed conditions of the Archean Earth. The rotation period is set to 17.5 hrs (adapted for an orbital period of 500 days according to Zahnle and Walker (1987); Bartlett and Stevenson (2016) - 1 day equal to 17.5 hrs). The spectrum of the star is calculated for 2.7 Ga and 1.0 AU from Claire et al. (2006) (see Figure 1). We define an atmosphere with 98% of N_2 and 1% of CO_2 for 1 bar at the surface. CH_4 has been added to the radiative contribution with different levels using the HITRAN 2012 database. The topography of the Archean Earth presumes a central continent. We define then a ocean planet with an equatorial supercontinent as in Charnay et al. (2013) (latitude $\pm$ 38°, longitude $\pm$ 56°).

The 1D version of the model uses a surface ocean, a surface mean albedo of 0.28, a mean solar zenith angle of 60° and an eddy diffusion coefficient vertical profile from Zahnle et al. (2006).

Photochemical losses from the atmosphere by methane oxidation in the GCM are balanced with a production flux at the surface. This flux is established by fixing the abundance of the species considered in the first layer of the GCM (formula (8)). It gathers all the surface contribution, such as organic carbon burial or input of reductants, which can be in a dynamical equilibrium with atmospheric chemistry. When the stationary regime is reached, we can quantify the total photochemical loss/production of a species as its integrated surface flux required to maintain constant its surface abundance. Several simulations are performed on a grid of oxygen and methane abundance at the surface. The calculated fluxes are used to determine the photochemical loss flux as a function of the variable oxygen and methane abundances at the surface.

Gregory et al. (2021) suggested to be cautious on the surface boundary conditions concerning a fixed mixing ratio or a fixed flux. While Gregory et al. (2021) does not describe the oxygen instability area with the fixed flux boundary condition, the fixed
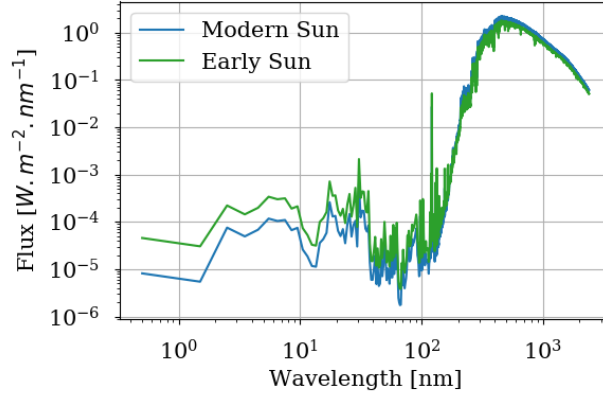
Figure 1. Stellar flux received by modern Earth computed for 0.0 Ga and 1.0 AU and stellar flux received by early Earth computed for 2.7 Ga and 1.0 AU from Claire et al. (2012).

mixing ratio boundary condition allow us to explore the full equilibrium states. Fixing the flux is indeed more physical (or in this case biological) than fixing mixing ratios as flux ratio can vary in time and space during the evolution toward the steady

125   state. But in the present study we wanted on purpose to determine the fluxes that correspond to a given steady state composition. The resulting fluxes are finally consistent with a 1/2 ratio driven by the oxygen and methane chemistry. Beyond this, additional simulation done by fixing the flux have shown some differences, which can not fully be explained by the analysis of Gregory et al. (2021) considering the 3D geometry of the surface but the homogeneous boundary condition for each approach. This need to be properly analyze in a study focusing only on this aspect, and could be done following this paper.

130   The GCM ensures the convergence of carbonaceous species by also fixing the CO_2 abundance at the surface to 1%. In addition, the GCM takes into account atmospheric escape according to the Catling et al. (2001) model. The H_2 abundance in the last layer of the GCM is updated according to the formula 6 thanks to the escape flux calculated by the formula 7.

$$H_2^{top} = H_2^{top} - \frac{\Delta t \times F_{H_2}}{\Delta^{n-1->n}z \times n^{top}} \tag{6}$$

$$F_{H_2} = 2.5 \times 10^{17} \times (H_2^{top} + 2CH_4^{top} + H_2O^{top}) \tag{7}$$

135   $$F_{O_2} = (O_2^{const} - O_2^{surf})\frac{\Delta^{1->2}z}{\Delta t}n^{surf} \tag{8}$$

Flux (surface or escape)	F_i [molecules.m^{-2}.s^{-1}]
Given surface value	O_2^{const} [ppmv]
First layer value	O_2^{surf} [ppmv]
Last layer value	H_2^{top} [ppmv]
Thickness of first layer	$\Delta^{1->2}z$ [m]
Thickness of last layer	$\Delta^{n-1->n}z$ [m]
Physical timestep	Δt [s]
Surface density	n^{surf} [molecules.m^{-3}]

3 Methane oxidation fluxes

The atmospheric oxygen loss is dominated by the oxidation of methane, formula (2). The oxidation of methane is catalyzed by OH radicals (Gebauer et al., 2017). These radicals are produced by the photochemistry of water vapor:

$$H_2O + h\nu \longrightarrow OH + H \tag{9}$$

$$H_2O + O(^1D) \longrightarrow OH + OH \tag{10}$$

The amount of water vapor in the troposphere is controlled by temperature in a 1D model with an infinite water reservoir on the surface but in a 3D dynamic model with dry continental surfaces, it also depends on the horizontal transport, evaporation and precipitations.

Photochemical processes depend on insolation and therefore on diurnal and seasonal variations. The formation of the ozone layer is a turning point for the photochemical balance. The ozone layer produces an UV shield, which limits the photochemical processes leading to methane oxidation and destroying oxygen. Oxygen can accumulate more efficiently and form more ozone. This positive feedback creates an oxygen instability which accounts for the sudden oxygenation of the atmosphere and may therefore be sensitive to the spatial distribution of ozone, and thus to the global 3D transport.

In this section, we compare the results between the 1D and 3D model on photochemical oxygen and methane losses at steady state. We compute the variation of vertical chemical pathways to methane oxidation as a function of the surface O_2 fixed abundance. We also analyze the spatial distribution of ozone. Finally, we examine how surface fluxes required to sustain a steady state depend on surface temperature.

3.1 From 1D to 3D models

We ran the 1D model until steady state for a range of O_2 from 10^{-7} to 10^{-3} volume mixing ratio and CH_4 from 10^{-6} to 10^{-3} volume mixing ratio . Figure 2 shows the total atmospheric O_2 loss (F_{O_2}) as a function of these two parameters. These results are consistent with the previous study of Zahnle et al. (2006).
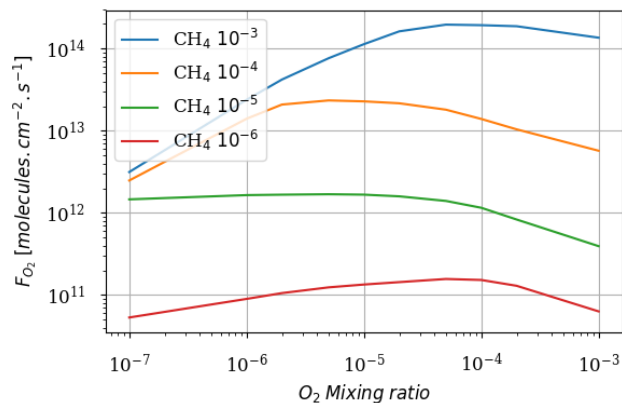
Figure 2. Oxygen atmospheric loss (F_{O_2}) as a function of surface O_2 for a surface CH_4 from 10^{-6} to 10^{-3}.

Figure 3 shows the atmospheric losses of oxygen (F_{O_2}) and methane (F_{CH_4}), the hydrogen escape flux (F_{H_2}) and the ozone column density computed with the 1D and 3D version of the GCM, for a methane abundance of 10^{-4} and an oxygen abundance grid between 10^{-7} and 10^{-3}. The results are obtained after the convergence of the model with less than 1% variation of the average last 50 time steps in 1D, last year in 3D compared to the previous one. This is done for the H_2, CO_2, CH_4 and O_2 surface flux, the H_2, CO_2, CH_4, O_2 and O_3 column density, the surface temperature and the Outgoing Longwave Radiation (OLR) and the Absorbed Shortwave Radiation (ASR). The surface fluxes at steady state in 3D present horizontal and seasonal variations and are averaged over the planetary surface and over one year (500 days). Timescales of the rise of oxygen are much larger than a year and the seasonal fluctuations are therefore not included in the following discussions. Discrepancies between 3D and 1D never exceed 10% for F_{O_2} and F_{CH_4}. However, the ozone column is always found larger in 1D, up to 5 times the mean column obtained with 3D. Others values of the arbitrary 1D zenith solar angle does not seem to explain this discrepancy. Figure 3 compare 1D simulations for both 40 and 60 degrees which present tiny differences compare to the 3D results. The average profiles of O_2, O_3, CO, CH_4, H_2 and water vapor found in 1D and 3D are presented in Figure 4. Differences can come either from averaging the UV irradiation geometry in 1D or from horizontal and vertical transport. A priori, the photochemical losses (F_{O_2} and F_{CH_4}) are not significantly modified (Figure 3) and the vertical transport seems responsible for these differences. The 3D vertical transport seems to transport species more efficiently than the 1D transport model which uses an Eddy coefficient from Zahnle et al. (2006) to mimic the 3D transport. In particular, this results in smaller vertical gradients with the 3D model (Figure 4).

Despite of the aforementioned small departures, we find that the 1D model reproduces the results of the more comprehensive 3D model.
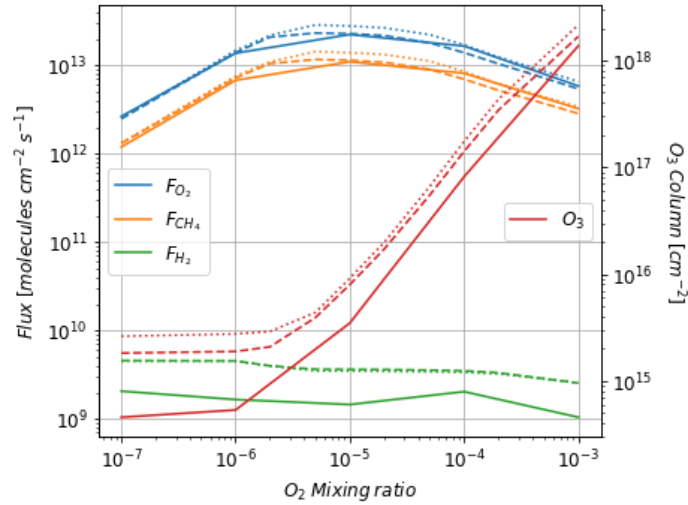
Figure 3. Oxygen atmospheric loss (F_{O_2}), methane atmospheric loss (F_{CH_4}), hydrogen escape (F_{H_2}) and O_3 column density as a function of surface O_2 for a surface CH_4 set up at 10^{-4}. Solid: results of 3D model (averaged over the surface and a year). Dashed: 1D results at a zenith solar angle of $60°$. Dot: 1D results at a zenith solar angle of $40°$.
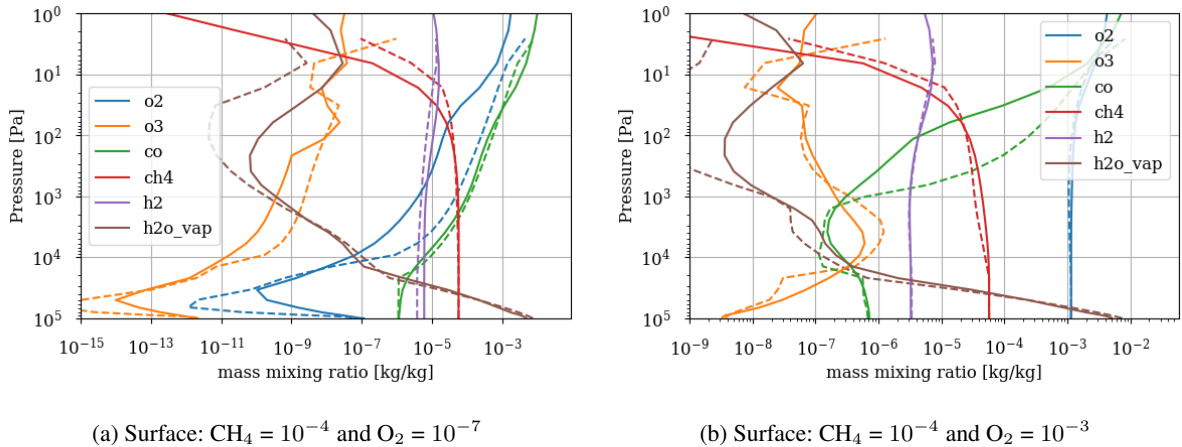
(a) Surface: $CH_4 = 10^{-4}$ and $O_2 = 10^{-7}$ (b) Surface: $CH_4 = 10^{-4}$ and $O_2 = 10^{-3}$

Figure 4. Species profile for 3D surface and annual average (solid) and 1D (dash) model.

3.2 Vertical distribution of O_2 losses

At steady state (averaging seasonal variations) O_2 photochemical losses compensate for the surface outgassing of O_2. The ratio 1/2 between F_{O_2} and F_{CH_4} (Figure 3) shows that the atmospheric losses of oxygen and methane are dominated by the methane oxidation reaction 2, which uses two molecules of O_2 for each molecule of methane (and forms one molecule of CO_2 and 2 molecules of H_2O). While oxygen molecules are mainly involved with CO and CO_2 cycle (Gebauer et al., 2017), CH_4 is

180

dominated by the methane oxidation. O_2, CO and CO_2 cycle is not a global loss of oxygen because there is no sources/losses of CO at the surface and consequently O_2 has a null balance, contrary to the methane oxidation. So, to analyze how losses of molecular oxygen are distributed in altitude, it is clearer to look at the methane loss, dominated by the oxidation of methane.

The Figure 5 represents the rate of methane destruction as a function of altitude and for different O_2 levels. As for their integrated value, the vertical profiles of F_{O_2} and F_{CH_4} are similar when computed with 1D and 3D models are similar. We distinguish the contribution to the loss of three main altitude domains : the troposphere, stratosphere and above. The losses are dominated, whatever the O_2 abundance, by the tropospheric contribution. In the appendix B, we identify empirically the main reaction pathways leading to a net methane oxidation 2. Figure 5 shows a migration of losses from the troposphere to the stratosphere when oxygen abundance increases. Catalysis by OH remains at the heart of the oxidation mechanism although a different reaction pathway is identified (Appendix B): as the stratospheric ozone becomes more abundant, the production of $O(^1D)$ through its photolysis increases:

$$O_3 + h\nu \longrightarrow O_2 + O(^1D) \tag{11}$$

which then initiates the production of OH through the reaction 10 instead of the $O(^1D)$ coming from O_2 photolysis. The stratospheric contribution is less efficient than the tropospheric one, that is why F_{O_2} decreases for the high abundances of oxygen. Finally, there are CH_4 and O_2 losses in the upper atmosphere (around 10 Pa), which are less sensitive to the surface O_2 level. This contribution is no longer dominated by the catalysis of OH but comes from the photolysis of methane. The different pathways are identified in appendix B. Due to the complexity of the chemistry, we developed suggested pathways which are relatively consistent with the work of Gebauer et al. (2017).
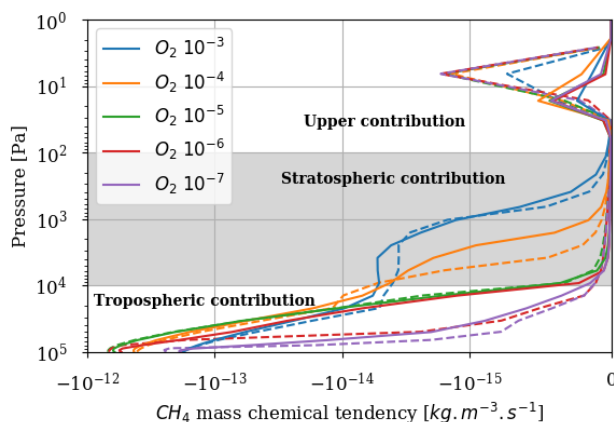
Figure 5. Methane photochemical losses as a function of altitude for several O_2 levels and a methane vmr of 10^{-4} at the surface. Solid: results of 3D model (averaged over the surface and a year). Dashed: 1D results.

3.3 Ozone

Figure 6 shows how the ozone column density during a year varies with latitudes from low to high pO_2. At low pO_2 we observe a maximum of ozone column density close to the poles during winter, while it switch to summer and at lower latitudes ($\sim 20°$) at high pO_2. For comparison, we computed the ozone column density for the current Earth with and without continent. Our simulation of the current Earth with continent reproduces quite well the present-day ozone distribution (Tian et al., 2010), with a maximum close to the north pole in March and at $50°$ south in October. The pole-ward transport of ozone in our simulation seems weaker than in reality, certainly due to the absence of the effect of gravity waves, which play a major role in the Brewer-Dobson circulation. By removing continent, the ozone maximum occurs later for both hemispheres, mostly due to the thermal inertia of the ocean. For such a case, the maximum of ozone occurs at the same season as the early Earth with high pCO_2 but at higher latitudes ($\sim 45°$). This is due to the faster rotation of the early Earth, limiting the latitudinal extension of the stratospheric circulation.

The 3D effects have no significant consequence on the photochemical losses of O_2. The decrease in F_{O_2} with increasing levels of O_2 above an O_2 vmr of 10^{-5} (Figure 3) is due to the formation of the ozone layer, due to UV shielding of the methane oxidation (Goldblatt et al., 2006; Zahnle et al., 2006). Figure 6 shows latitudinal variation relatively less than a factor 2, which have a tiny impact on the ozone lifetime and the photochemistry, and figure 7 shows that ozone is relatively homogeneous over the whole planet making 1D modeling relevant. Nevertheless, there are some variations of the O_3 column with latitude and related variations of the biologically harmful UV flux reaching the surface (Figure 8). This non-homogeneous opacity of the ozone UV shield may be important for the evolution and distribution of organisms living at the surface.

3.4 Surface temperature effect

The resulting tropospheric temperature profile , calculated in both 1D and 3D models, follows a moist/dry adiabat that controls the vertical profile of water vapour, which, in turn, affects the greenhouse warming. Since this water vapor is the source of OH, catalyzer of methane oxidation, this interplay suggests a possible link between surface temperature and photochemical losses of CH_4 and O_2, which we investigate here.

The previous results (Figure 3) were obtained with a surface temperature close to 280 K, whatever the oxygen abundance at the surface and an abundance of methane of 10^{-4}. The surface temperature is the same because all the parameters are the same (rotation period, obliquity, solar input, surface composition (water/continent), continental albedo, etc...) and main greenhouse gases (CO_2, CH_4) are not changed depending on the oxygen level.

As a first test to assess the effect of surface temperature, we use the 1D model with a surface surface temperature forced to remain at 220 K (by setting to zero the heating/cooling rate of the surface). This is the approximate surface temperature that would be reached by the 1D model with a frozen start, although the actual value would depend on the level of greenhouse CH_4. This way we can evaluate the impact of a snowball event on the photochemistry. Figure 9 shows that photochemical losses decrease with the temperature. How strong this decrease is depends on the O_2 level, the drop being the largest around the maximum of F_{O_2}, so for a vmr of O_2 around 10^{-5}. At this O_2 level, the photochemical losses occur entirely in the troposphere.
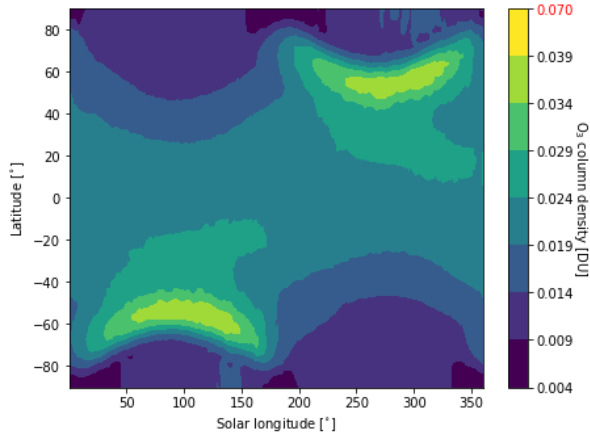
(a) Surface: $CH_4 = 10^{-4}$ and $O_2 = 10^{-6}$
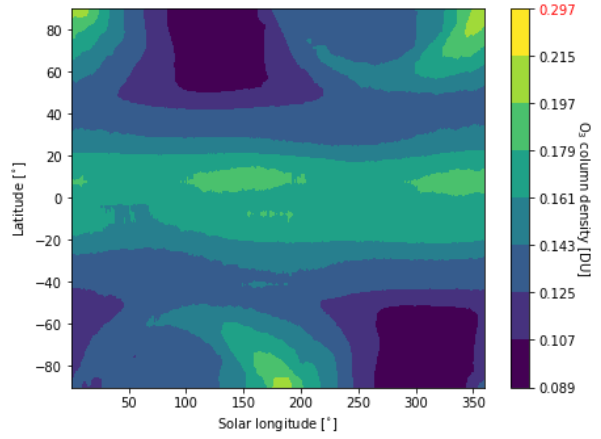
(b) Surface: $CH_4 = 10^{-4}$ and $O_2 = 10^{-5}$
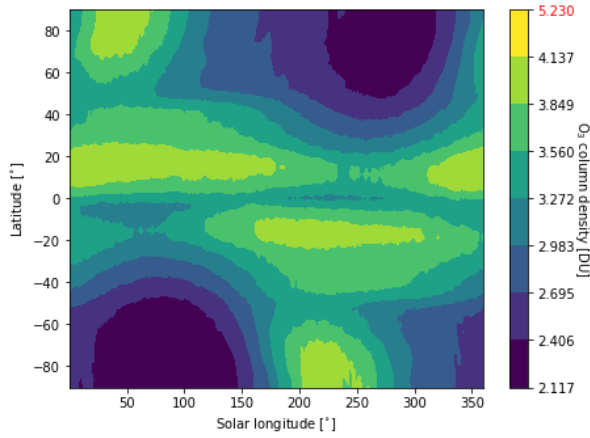
(c) Surface: $CH_4 = 10^{-4}$ and $O_2 = 10^{-4}$
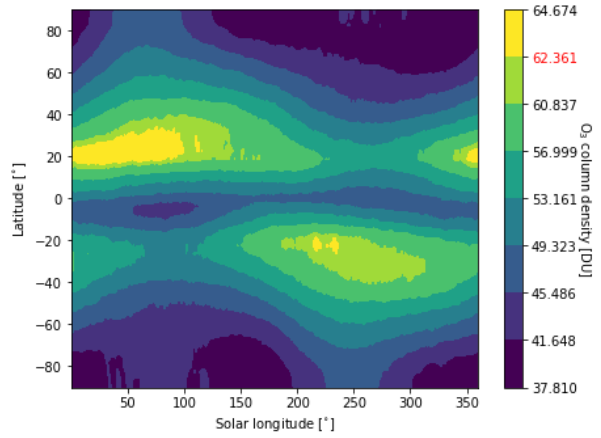
(d) Surface: $CH_4 = 10^{-4}$ and $O_2 = 10^{-3}$
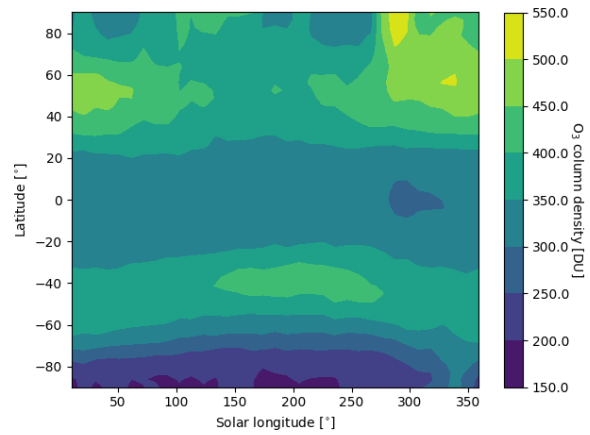
(e) Continental Earth 3D GCM
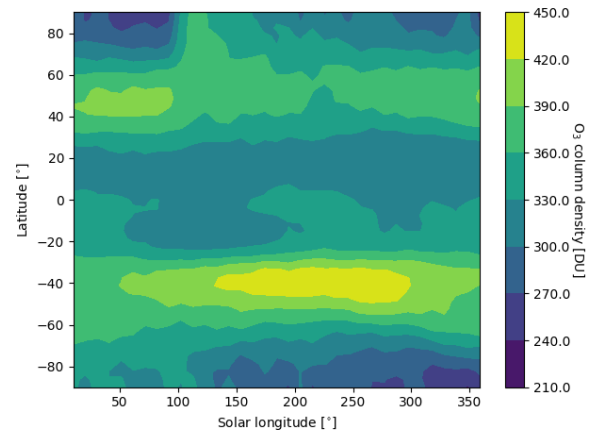
(f) Aqua Earth 3D GCM

Figure 6. Ozone column density zonal mean over 13 years for early earth, over one year for an actual simulated continental and aqua Earth. 1D simulated early Earth value are pointed in red.
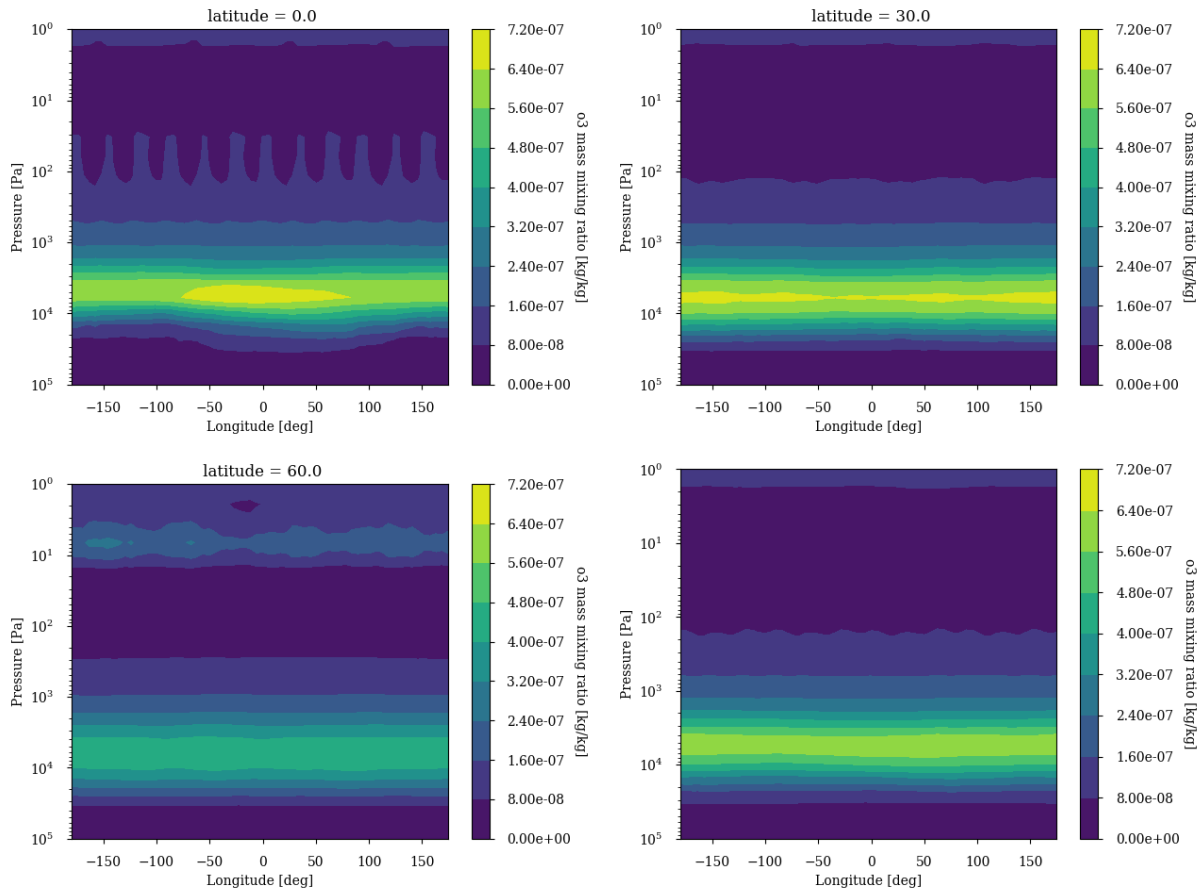
Figure 7. Ozone annual average longitudinal profile for latitude $0°$, $30°$, $60°$ and latitudinal average. Surface: $CH_4 = 10^{-4}$ and $O_2 = 10^{-3}$

Figure 10 compares the vertical profiles of methane photochemical losses for a surface temperature of 280 K and 220 K and for different oxygen abundances at the surface. We see that the influence of surface temperature on the losses is located in the troposphere. Thus, the larger the tropospheric contribution, the larger the decrease in losses. The stratospheric thermal profile

235 and the troposause (the cold trap that controls the transport of water vapor to the stratosphere) show little response to a decrease of surface temperature from 280 K to 220 K (see Figure 13). As a consequence only the tropospheric chemistry is affected.

The main implication of this result is that, under conditions of a global glaciation, the oxygen instability is triggered for an oxygen abundance/flux about an order of magnitude lower. For a given O_2 flux, glacial conditions should favor the switch from an oxygen-poor to an oxygen-rich atmosphere. During glaciations, however, environments able to provide both light and

240 liquid water are considerably limited making likely a considerable drop in the photosynthetic production of O_2 and the burial of biomass.
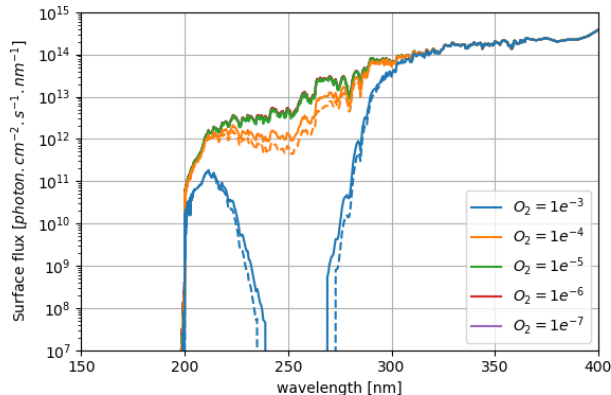
Figure 8. Stellar flux reaching the surface for several surface oxygen and surface methane of 10^{-4}. Results of 3D model surface and annual average (solid) and 1D model (dash).
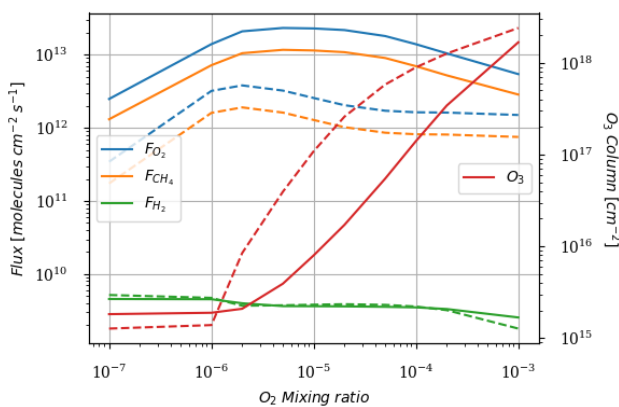
Figure 9. Surface oxygen (F_{O_2}) and methane (F_{CH_4}) fluxes, hydrogen escape (F_{H_2}) and O_3 column density as a function of surface O_2 for a surface CH_4 set up at 10^{-4}. Results for 1D model surface temperature 280K (solid) and 220K (dashed).
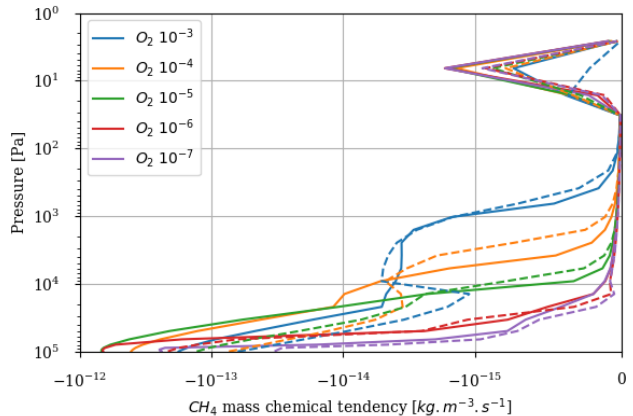
Figure 10. Methane photochemical losses as a function of altitude for several O_2 levels and a surface CH_4 vmr of 10^{-4}. Results from 1D modeling and for a surface temperature of 280K (solid) and 220K (dashed).

The temperature trend of oxygen losses is determined. These losses are calculated using the 1D model by setting different surface temperatures for a methane abundance of 10^{-4} and an oxygen abundance of 10^{-5} at the surface. Figure 12 shows F_{CH_4} (equivalent to $\frac{1}{2}F_{O_2}$) as a function of surface temperature. We observe an order of magnitude increase in losses per 50 K. The discontinuity at 273 K is artificially produced by the change of albedo at the surface between ice-free oceans (albedo = 0.07) and fully ice-covered oceans (albedo = 0.65). The increase in albedo below 273 K reflects more UV flux and increases photochemical losses in the troposphere. The 3D model smooths this effect by gradually freezing the ocean at the surface. We use the slow convergence of the 3D model towards a frozen state. The photochemical equilibrium is established on a time

(a) Surface: $CH_4 = 10^{-4}$ and $O_2 = 10^{-6}$

(b) Surface: $CH_4 = 10^{-4}$ and $O_2 = 10^{-5}$

(c) Surface: $CH_4 = 10^{-4}$ and $O_2 = 10^{-4}$

(d) Surface: $CH_4 = 10^{-4}$ and $O_2 = 10^{-3}$
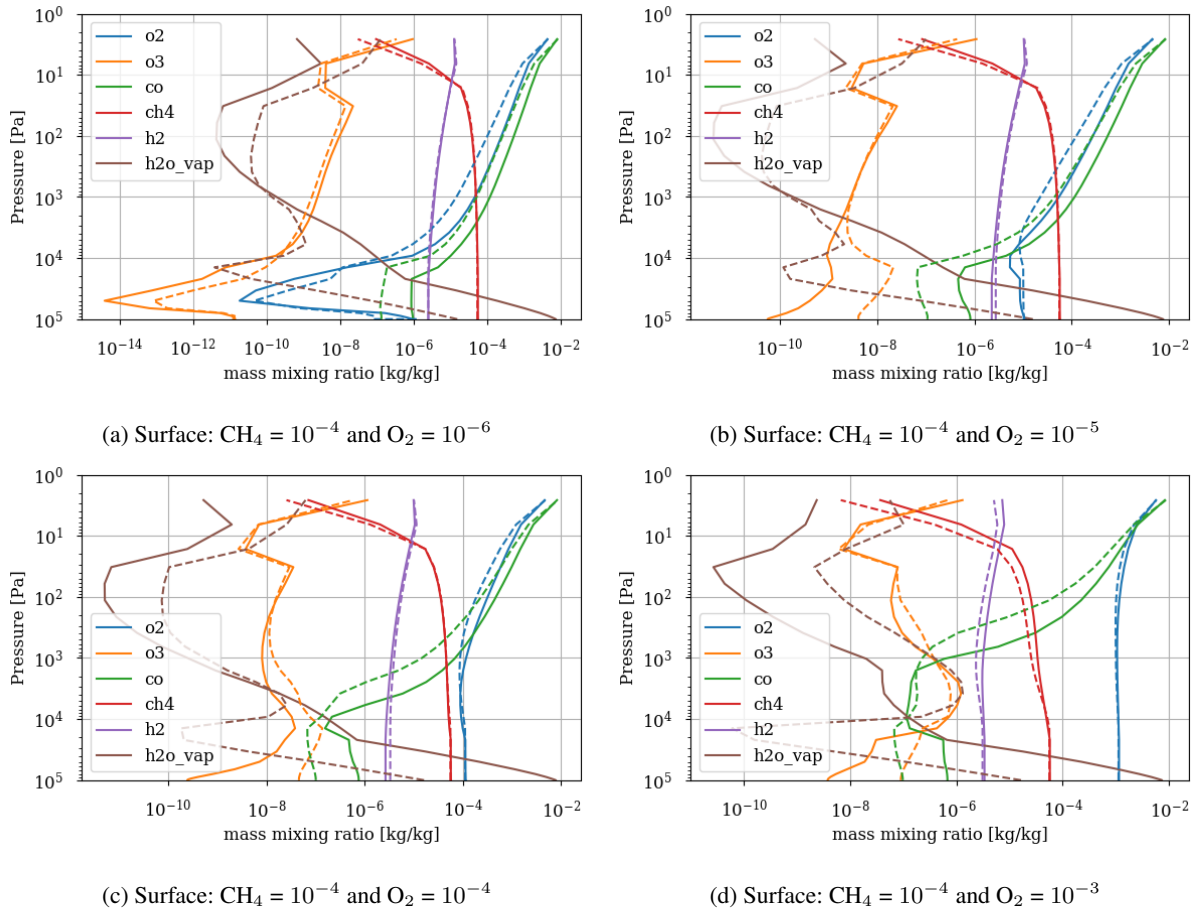
Figure 11. Species profile for 1D model surface temperature 280K (solid) and 220K (dashed).

scale of a few years, whereas the progressive freezing of the surface takes place over several decades. A quasi-stationary state
of species abundance in the atmosphere and consequently of atmospheric losses is rapidly established. During freezing on a
longer time scale, the evolution of temperature and oxygen losses in their quasi-stationary state is recorded to establish the link
between oxygen losses and temperature, see Figure 12. The 3D model converges to a frozen state where the sea ice extends
from the poles to 20-25°N/S. The coverage is about 60-65%, as observed in Charnay et al. (2013), and the surface temperature
converges to 230 K. A cold start with a completely frozen surface is then performed to evaluate the impact of the 3D model
following a global glaciation. The results Figure 12 show that in addition to the smoothing of the albedo effect, the trend
is weaker than the 1D model. At the root of this difference is the difference in transport between the two models. The 3D
model mixes the tropospheric temperature more efficiently, warming the troposphere and reducing the impact of a cooling on
atmospheric losses, see Figure 13.
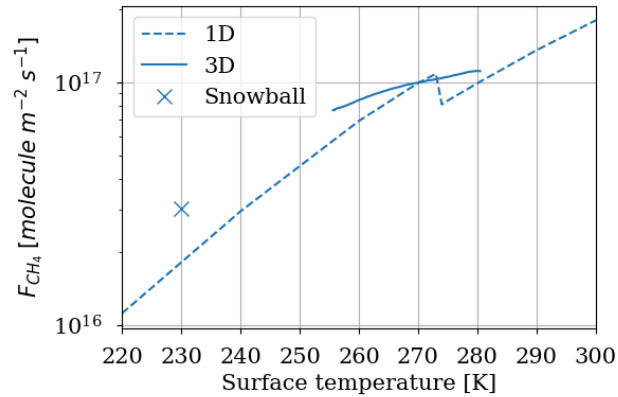
Figure 12. F_{CH_4} depending on the surface temperature. Results of 3D model surface and annual average (solid and mark for snowball) and 1D model (dash). Surface: $CH_4 = 10^{-4}$ and $O_2 = 10^{-5}$.
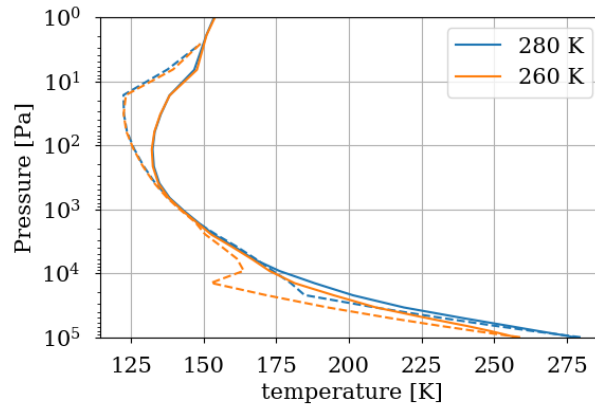
Figure 13. Temperature profile for a surface temperature of 280 K and 260 K. Results of 3D model surface and annual average (solid) and 1D model (dash).

Temperature appears to have a significant impact on atmospheric loss Between a temperate state and an ice age, oxygen losses can vary by a factor of 2 to 4. Oxygen abundance and methane abundance can accumulate more in the atmosphere during an ice age. The consequences of ice ages on the temporal evolution of oxygen and methane during the GOE are studied in the following by considering this new trend.

4 Temporal evolution, overshoot and glaciation events

After the GOE, a carbon-13 isotopic variation of nearly 15 ‰ is observed (Lyons et al., 2014). This event is called the Loma-gundi event (Bachan and Kump, 2015). Although the dynamics of the oxygenation process remain uncertain, this event suggests

an over-oxygenation of the atmosphere (Catling and Zahnle, 2020). Other evidence supports this phenomenon, such as the evolution of the δ^{34}S fraction of carbonate-associated sulfates (Planavsky et al., 2012; Schröder et al., 2008) or fluctuations in the degree of uranium enrichment in organic-rich shales (Partin et al., 2013). An increase in overall oxygen productivity followed by a decrease would seem to account for this over-oxygenation (Harada et al., 2015; Holland and Bekker, 2012; Hodgskiss et al., 2019). Nevertheless, we have seen previously that a global glaciation phenomenon can significantly decrease the atmospheric oxygen losses. It is therefore not impossible that Huronian glaciations could also have had an impact on atmospheric over-oxygenation during the global oxygenation process. In order to study the dynamics of over-oxygenation, a time evolution equation model is established based on the equations of Goldblatt et al. (2006), Claire et al. (2006) and adjusted to take into account variations in primary oxygen productivity and atmospheric losses. We compare the previous Goldblatt et al. (2006) parametrisation for atmospheric loss with the GCM interpolated function on the time evolution without an over-oxygenation using the time evolution equation model established. We then apply this model to reproduce the over-oxygenation and the fluctuations brought by glaciations.

4.1 Equations model

The temporal evolution of oxygen and methane abundance during the GOE is modeled by the Goldblatt et al. (2006) equations. They relate atmospheric losses, described in section 3, to surface contributions associated with biogeochemical exchanges. Goldblatt et al. (2006) propose for this biosphere model a parameterization of atmospheric losses according to $\Psi_{O_2}[CH_4]^{0.7}$ where $\Psi_{O_2} = 10^{a_1\psi^4 + a_2\psi^3 + a_3\psi^2 + a_4\psi + a_5}$, $\psi = log([O_2])$, $a_1 = 0.0030$, $a_2 = -0.1655$, $a_3 = 3.2305$, $a_4 = -25.8343$ and $a_5 = 71.5398$. Goldblatt et al. (2006) also estimate the value of the different parameters (see Table 1). A set of values is associated with a steady state of oxygen and methane abundances. Depending on the value of the flux of reductant r, one is on a state of oxygen-poor or oxygen-rich equilibrium. In order to study the temporal evolution between these two equilibrium states, we use the results of Claire et al. (2006) to establish a temporal evolution of the flux of reductant r (Figure 14). We introduce this temporal evolution in the equations of Goldblatt et al. (2006) to reproduce the dynamics of oxygenation. Finally, we introduce a coefficient α_N (≥ 1) to model a photosynthetic over-productivity responsible for the over-oxygenation, as well as a coefficient α_Ψ (≤ 1) to model the decrease of the atmospheric losses during a glaciation. The evolution of the abundance of oxygen, methane and buried carbon is then described by equations:

$$\frac{d[CH_4]}{dt} = \alpha_N \frac{1}{2}\Omega_{O_2}N + \frac{1}{2}\Omega_{O_2}r - s[CH_4] - \alpha_\Psi \frac{1}{2}\Psi_{O_2}[CH_4]^{0,7} - \frac{1}{2}\Omega_{O_2}(\beta(N+r) - wC) \tag{12}$$

$$\frac{d[O_2]}{dt} = \alpha_N \Omega_{O_2}N - (1 - \Omega_{O_2})r - s[CH_4] - \alpha_\Psi \Psi_{O_2}[CH_4]^{0,7} - (1 - \Omega_{O_2})(\beta(N+r) - wC) \tag{13}$$

$$\frac{dC}{dt} = \beta(N+r) - wC \tag{14}$$

Terms	Description	Values
Atmospheric fluxes		
$\Psi_{O_2}[CH_4]^{0,7}$	Photochemical oxidation	Parametrization
$s[CH_4]$	Atmospheric escape	$s = 2.03 \times 10^{-5}\ yr^{-1}$
Surface fluxes		
N	Oxygenic photosynthesis	3.75×10^{14} mol O_2 equiv.yr^{-1}
Ω_{O_2}	Fraction of O_2 produced that reaches the atmosphere	$\Omega_{O_2} = (1-\gamma)(1-\delta)$
γ	Fraction consumed	$\gamma = [O_2]/(d_\gamma + [O_2])$
	by heterotrophic respirers	$d_\gamma = 1.36 \times 10^{19}$ mol
δ	Fraction consumed	$\delta = [O_2]/(d_\delta + [O_2])$
	by methanotrophs	$d_\delta = 2.73 \times 10^{17}$ mol
w	Bulk organic carbon weathering rate	$6 \times 10^{-9}\ yr^{-1}$
β	Fraction of organic carbon burial	2.66×10^{-3}
r	Ferrous iron reducing material	$F_V + F_M + F_W - F_B$
	Anoxygenic photosynthesis	mol O_2 equiv.yr^{-1}
F_V	Volcanic flux of reductants	$1.59 \times 10^{10} \left(\frac{3.586}{3.586-t}\right)^{0.17}$
F_M	Metamorphic outgassing of reductants	$6.12 \times 10^{11} \left(\frac{4.11}{4.11-t}\right)^{0.7}$
F_B	Burial	$1.06 \times 10^{12} \left(\frac{3.653}{3.653-t}\right)^{0.2}$
F_W	Oxidative weathering	$3.7 \times 10^4 [O_2]^{0.4}$

Table 1. Equation dependencies and values from Goldblatt et al. (2006). Reductant model from Claire et al. (2006) with time t [Gyrs] and amount of oxygen $[O_2]$ [mol].
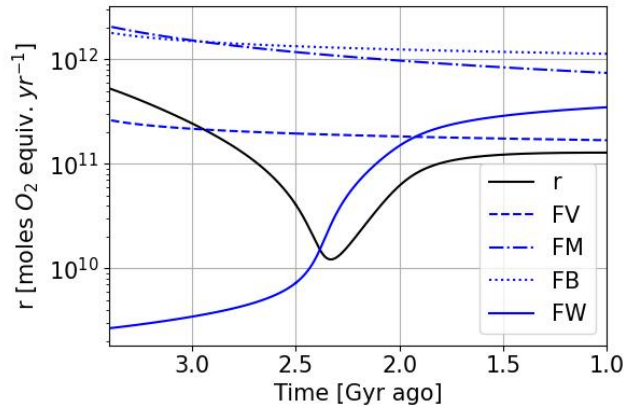
Figure 14. Temporal evolution of the reductant contributions (see Table 1) with $\alpha_i = 1$ and using for oxygen atmospheric loss (F_{O_2}) the Goldblatt et al. (2006) parametrization.

295   where the different terms and values are detailed in Table 1.

The size and shape of the over-oxygenation is uncertain, as are the possible variations in oxygen sources and losses during this process. We then arbitrarily define a log-polynomial fit for the time evolution of the parameters $\alpha_i = e^{(a(t-t_0)^{2p}+b)}$ ($\alpha_i = \alpha_N$ or α_Ψ). When there is no deviation from the initial model the values of α_i are equal to 1. The variation of the α_i parameters is triggered in a way that is consistent with the predictions of previous studies on the evolution of primary productivity and ice

300   ages.

4.2   Dynamics with constant temperature and constant primary productivity

The Goldblatt et al. (2006) parameterization for atmospheric oxygen loss as a function of oxygen and methane abundance is compared (Figure 15) to the results obtained with the 1D GCM, which are shown to be similar to the 3D model. The parameterization established by Goldblatt et al. (2006) does not seem to correctly capture the methane dependence. This

305   variation is not independent of oxygen abundance and cannot be described by a constant power x of methane abundance $[CH_4]^x$. At high oxygen abundances ($> 10^{-4}$) the variation seems to increase with increasing methane, and conversely at lower oxygen abundances ($< 10^{-4}$). An asymptote appears to emerge at low oxygen abundances for the highest methane abundances ($> 10^{-5}$). This behaviour is already seen in Zahnle et al. (2006).
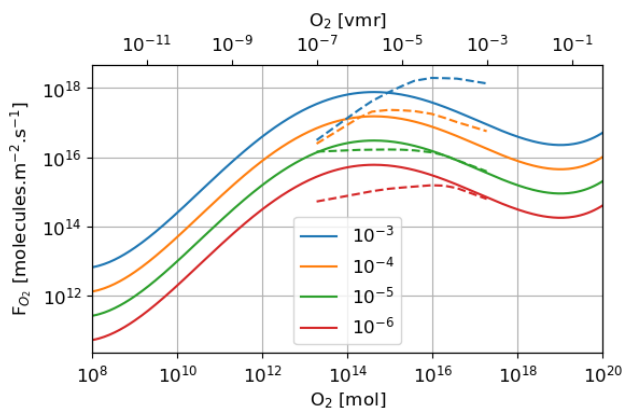
Figure 15. Oxygen atmospheric loss (F_{O_2}) depending on oxygen and methane (label in [vmr]). Goldblatt et al. (2006) parametrization (solid) and GCM 1D results (dash).

Figure 16 shows the equilibrium states as a function of the total reductant parameter r with the Goldblatt et al. (2006)

310   parameterization and an interpolation of the 1D GCM results for the atmospheric losses. These curves show the stable and unstable equilibrium states of the atmosphere. They justify the rapid switch from an oxygen-poor to an oxygen-rich state. The flux of reductant that triggers the instability varies from about $1. \times 10^{10}$ to $3. \times 10^{10}$ mol O_2 equiv. yr^{-1} with the interpolation of the 1D GCM results. The asymptotic behaviour of the atmospheric losses calculated with the 1D GCM at low oxygen and

high methane (high r) levels, can be seen on the equilibrium states with a approximatevly constant value at those levels. This
behaviour remains uncertain.
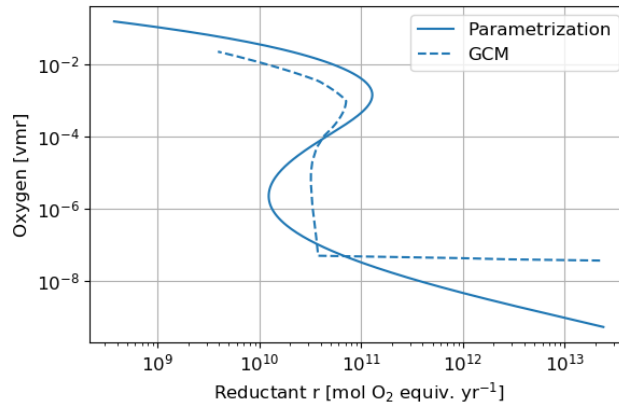
Figure 16. Equilibrium states of the time evolution equation model depending on the reductant parameter r. Oxygen atmospheric loss (F_{O_2})
Goldblatt et al. (2006) parametrization (solid) and GCM 1D results (dash).

A time evolution of oxygen and methane abundance with these two atmospheric loss models (Figure 17) shows that with the
interpolation of 1D GCM results oxygenation is faster. The equilibrium positions Figure 16 show that indeed the amount of
oxygen is more sensitive to the flux of reductant. Oxygenation therefore occurs for a smaller variation of the reductant flux. As
the methane abundance is directly related to the reductant flux ($[CH_4] = \frac{r}{s}$), we also observe a smaller variation of the methane
abundance during oxygenation.
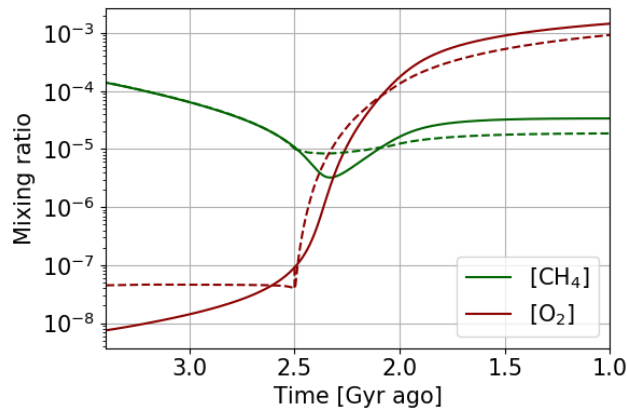
Figure 17. Temporal evolution of oxygen and methane with $\alpha_i = 1$. Oxygen atmospheric loss (F_{O_2}) Goldblatt et al. (2006) parametrization
(solid) and GCM 1D results (dash).

4.3 Long overshoot with variable primary productivity

We model a long variation over 400 million years of the primary productivity, parameter α_N, with a first phase of over-production before a return to the initial production. We represent Figure 18 the reference evolution for constant α_N equal to 1, as well as two different intensities of over-productivity with a maximum at 2 and 10 times the initial productivity. The reference model is in good agreement with the results of Goldblatt et al. (2006) and Claire et al. (2006). We observe a variable over-oxygenation depending on the intensity of the primary productivity variation, but also an over-abundance of methane. The primary productivity corresponds to a photosynthetic production of oxygen but also of organic matter, transformed then into methane by the methanogens. Consequently, the production of methane is increased as well as that of oxygen. Such an over-abundance of methane is not highlighted by previous studies, nor by the geological record. It is difficult to constrain the amount of methane at that time. This scenario is therefore possible, although one could also imagine that oxygen enrichment of the atmosphere limited the conversion of organic matter into methane. A conversion that is carried out by methanogens, developing more favorably in a reducing environment.
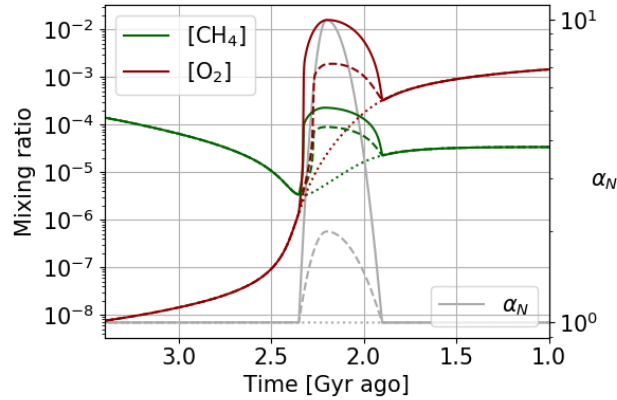
Figure 18. Oxygen and methane temporal evolution. Models α_N constant equal 1, reaching a factor 2 and reaching a factor 10.

This temporal evolution is identical if we model an inverse variation of atmospheric losses ($\alpha_\Psi = \frac{1}{\alpha_N}$), corresponding to a glaciation event of 400 million years. This scenario is less likely since there are several shorter glaciation events, called Huronian glaciations (Young et al., 2001). In addition, a change in primary productivity provides a link to the positive anomaly in carbon-13 isotope fractionation (Lyons et al., 2014). By using the model of the evolution of the isotopic ratio of Goldblatt et al. (2006), we can evaluate the impact of the variation of primary productivity or atmospheric losses on this ratio:

$$f = \frac{\delta_{carb} - \delta_i}{\delta_{carb} - \delta_{org}} \tag{15}$$

where f is the fraction of buried volcanic carbon, δ_{carb} is the carbon-13 isotope ratio $\delta^{13}C$ for carbonates, δ_i is the carbon-13 isotope ratio $\delta^{13}C$ for volcanic carbon, and δ_{org} is the carbon-13 isotope ratio $\delta^{13}C$ for organic carbon. The fraction of buried

volcanic carbon can be described by the biosphere model based on the fraction C of buried carbon where $C \sim \frac{\beta}{w}(N+r)$. We establish the approximation that $f \; \alpha \; (N+r)$. Goldblatt et al. (2006) defines the initial state during the Archean with $\delta_{carb} = 0$ ‰, δ_i = -6 ‰ and δ_{org} = -30 ‰ giving $f = 0.2$. With this initial state, we determine the relation of proportionality between f and $(N+r)$, then we evaluate the evolution of the isotopic fractionation of the carbonates δ_{carb} during the temporal evolution

345   of the oxygen and methane abundance thanks to the formula:

$$\delta_{carb} = \frac{\delta_i - f \times \delta_{org}}{1 - f} \tag{16}$$

Figure 19 represents the evolution of δ_{carb} as a function of time for the time evolution models established with a primary over-productivity reaching a factor of 2 and the inverse evolution of atmospheric losses. A primary over-productivity is consistent with the anomaly of about 15 ‰ measured in contrast to the decrease in atmospheric losses.
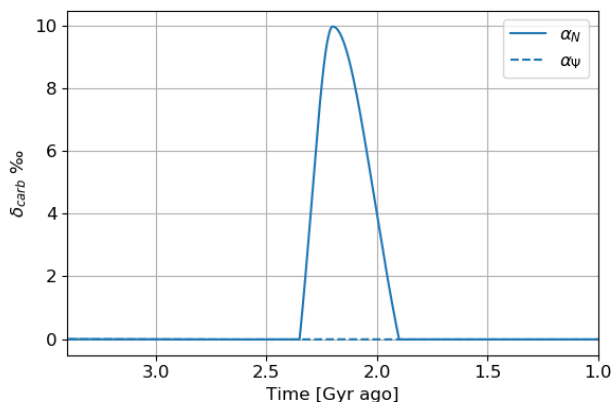
Figure 19. Temporal evolution of δ_{carb}. Models with α_N reaching a factor 2 and α_Ψ reaching a factor 0.5.

350   ## 4.4   Short overshoot with variable temperature

The Huronian glaciations represent several glacial events that took place during the oxygenation of the atmosphere at the beginning of the Proterozoic. The model of the α_Ψ parameter variation over 400 million years is therefore not consistent with the episodic nature of these glaciations. To reflect the impact of these glaciations on atmospheric losses, an episodic variation over shorter times during the oxygenation period can be established. Figure 20 presents the temporal evolution of oxygen and

355   methane following this adjustment. We observe the punctual over-oxygenations linked to the variations of α_Ψ with a global trend that follows the temporal evolution of the initial model where $\alpha_i = 1$. We note, during the over-oxygenation, an increase in the methane abundance. This increase in greenhouse gases can trigger the thawing of the surface. During the thawing, the surface temperature increases causing an increase in atmospheric losses by oxidation of methane. This is why the amount of methane decreases again. This negative feedback, coupled with the hysteresis phenomenon between the frozen and warm state

360   of the surface, could be one of the key factors to explain the cyclic character of Huronian glaciations.
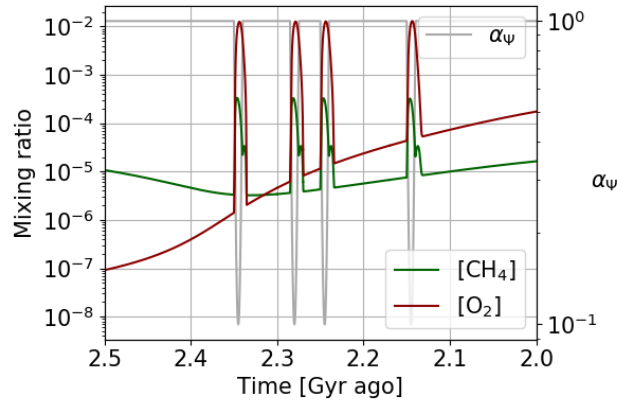
Figure 20. Oxygen and methane temporal evolution. Models α_Ψ reaching a factor 0.1 on shorter timescales.

Figure 21 shows the complete model for over-oxygenation with a 400 million year variation in primary productivity and a maximum factor of 2, as well as a fluctuation provided by shorter time scale variations in atmospheric losses due to Huronian glaciations with a maximum factor of 0.5. This coupling is not intended to exactly reproduce what happened during the GOE but to highlight both effects on the evolution of oxygen and methane during this event.
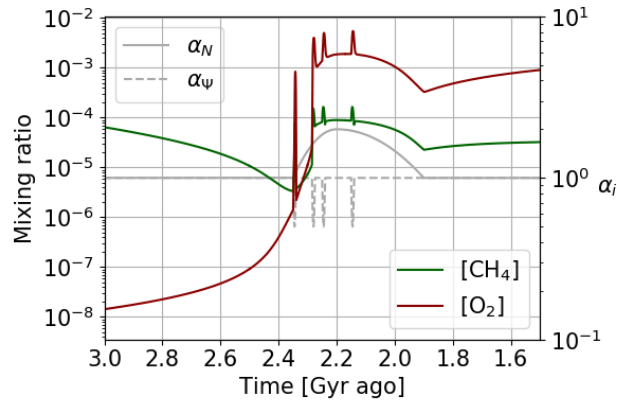
Figure 21. Oxygen and methane temporal evolution. Models α_N reaching a factor 2. Models α_Ψ reaching a factor 0.5 on shorter timescales.

365 5   Conclusions

The atmospheric equilibrium states during the Archean and the Proterozoic has been establish for the first time using a 3D photochemical-climate model. Despite some 3D transport discrepancies the atmospheric-surface equilibrium fluxes of methane and oxygen are not significantly different from a 1D model as it has been done in Zahnle et al. (2006) or Gebauer et al. (2017).

Following, the (photo)chemical equilibrium pathways have been determined depending on the altitude. It highlights the evolution of the tropospheric and stratospheric contribution depending of the oxygen levels. What remains however constant is the important link with the OH molecules which catalyze the methane oxidation. Because of that, we found a crucial dependency of the surface fluxes equilibrium with the surface temperature. This temperature dependence is sensitive to the 3D transport and appears weaker in 3D than in 1D. However, a global glaciation could reduce the oxygen atmospheric losses by a factor 2 to 10. Taking this new contribution into account in a time evolution model, we show that glaciations bring fluctuations in oxygen and methane abundance with an overshoot during glaciations. The increase in methane following glaciation produces an additional greenhouse effect that could eventually lead to deglaciation. This warming increases again the atmospheric losses of methane and it is possible to establish a cycle of glaciation-deglaciation. Few evidences of methane (Lowe and Tice, 2004; Cadeau et al., 2020) have been yet discovered but it could explain how the planet has been warmed up enough to terminate the glaciation thanks to the methane greenhouse effect. The feedback between the glaciation and the methane evolution coupled with the glaciation hysteresis process might also explain the multiple glaciations known as the Huronian glaciations. More generally, the link between temperature and photochemical processes shows that a decrease in temperature favors the oxygenation of the atmosphere. Without falling into a global glaciation, phenomena such as the decrease of the atmospheric CO_2 or the emergence of continents induce a decrease of temperature favorable to the oxygenation of the atmosphere.

Beyond the temperature, the UV-Visible stellar radiation received by the planet controls the photochemical processes and the quantity of ozone, essential for the oxygenation phenomenon of the atmosphere. A red dwarf such as TRAPPIST-1a presents a spectral distribution in favor of the UV radiation with respect to the visible radiation which favors the accumulation of ozone. The 1D study of Gebauer et al. (2018) shows that around such red dwarfs the oxygenation of the atmosphere is triggered for lower atmospheric oxygen levels and surface oxygen flux. These irradiation conditions then favor the oxygenation of the atmosphere. A compact system such as TRAPPIST-1 has presumably synchronous planets (Vinson and Hansen, 2017), which brings an interest to use 3D models. The permanent dichotomy between day and night side brings an important variation of temperature (Leconte et al., 2013) and photochemical processes. The red dwarfs represent the majority of the stars and would thus shelter the majority of the planets. It is then necessary to understand how an oxygenated atmosphere could evolve around these planets. For this, 3D models will be necessary to capture the effect of a synchronization.

Appendix A: Chemical network

Table A1. Chemical network with rate coefficients and references used to model the early Earth.

Units are s^{-1} for photolysis reactions, $cm^3.s^{-1}$ for two-body reactions, and $cm^6.s^{-1}$ for three-body reactions. [M] correspond to the density in molecules.cm^{-3}. If k_0 and k_∞ specified, the formula is $\frac{k_0[M]}{1+\frac{k_0}{k_\infty}[M]}0.6^{[1+[log_{10}(\frac{k_0}{k_\infty}[M])]^2]^{-1}}$. If $k_{1a,0}$, $k_{1b,0}$, $k_{1a,\infty}$ and F_c specified, the

formula is $k_{1a,0}\frac{1+\frac{k_{1b,0}}{k_{1a,\infty}-k_{1b,0}}}{1+\frac{k_{1a,0}}{k_{1a,\infty}-k_{1b,0}}}F_c^{[1+[log(\frac{k_{1a,0}}{k_{1a,\infty}-k_{1b,0}})]^2]^{-1}} + k_{1b,0}\frac{1}{1+\frac{k_{1a,0}}{k_{1a,\infty}-k_{1b,0}}}F_c^{[1+[log(\frac{k_{1a,0}}{k_{1a,\infty}-k_{1b,0}})]^2]^{-1}}$

Reaction								Rate Coefficient	Reference
O_2	+	$h\nu$	$\longrightarrow$	O	+	O		$J_{O_2 \rightarrow O}$	Ogawa and Ogawa (1975)
O_2	+	$h\nu$	$\longrightarrow$	O	+	$O(^1D)$		$J_{O_2 \rightarrow O(^1D)}$	and Lewis et al. (1983)
									and Gibson et al. (1983)
									and Minschwaner et al. (1992)
									and Yoshino et al. (1988)
									and Fally et al. (2000)
CO_2	+	$h\nu$	$\longrightarrow$	CO	+	O		$J_{CO_2 \rightarrow O}$	Chan et al. (1993)
CO_2	+	$h\nu$	$\longrightarrow$	CO	+	$O(^1D)$		$J_{CO_2 \rightarrow O(^1D)}$	and Stark et al. (2007)
									and Yoshino et al. (1996)
									and Parkinson et al. (2003)
									and Lewis and Carver (1983)
O_3	+	$h\nu$	$\longrightarrow$	O_2	+	O		$J_{O_3 \rightarrow O}$	Sander et al. (2006)
O_3	+	$h\nu$	$\longrightarrow$	O_2	+	$O(^1D)$		$J_{O_3 \rightarrow O(^1D)}$	
H_2O	+	$h\nu$	$\longrightarrow$	OH	+	H		J_{H_2O}	Mota et al. (2005)
									and Chung et al. (2001)
									and Thompson et al. (1963)
H_2O_2	+	$h\nu$	$\longrightarrow$	OH	+	OH		$J_{H_2O_2}$	Schurgers and Welge (1968)
									and Demore et al. (1997)
HO_2	+	$h\nu$	$\longrightarrow$	OH	+	O		J_{HO_2}	Sander et al. (2003)
CH_4	+	$h\nu$	$\longrightarrow$	CH_3	+	H		$J_{CH_4 \rightarrow CH_3}$	Kameta et al. (2002)
CH_4	+	$h\nu$	$\longrightarrow$	$^1CH_2$	+	H_2		$J_{CH_4 \rightarrow ^1CH_2}$	and Chen and Wu (2004)
CH_4	+	$h\nu$	$\longrightarrow$	$^3CH_2$	+	H	+ H	$J_{CH_4 \rightarrow ^3CH_2}$	and Lee et al. (2001)
CH_4	+	$h\nu$	$\longrightarrow$	CH	+	H_2	+ H	$J_{CH_4 \rightarrow CH}$	
CH_2O	+	$h\nu$	$\longrightarrow$	CHO	+	H		$J_{CH_2O \rightarrow CHO}$	Sander et al. (2011)
CH_2O	+	$h\nu$	$\longrightarrow$	CO	+	H_2		$J_{CH_2O \rightarrow CO}$	

Reaction								Rate Coefficient	Reference
C_2H_6	+	$h\nu$	$\longrightarrow$	CH_4	+	$^1CH_2$		$J_{C_2H_6 \longrightarrow CH_4}$	Lee et al. (2001)
C_2H_6	+	$h\nu$	$\longrightarrow$	C_2H_2	+	H_2	+ H_2	$J_{C_2H_6 \longrightarrow C_2H_2}$	
C_2H_6	+	$h\nu$	$\longrightarrow$	C_2H_4	+	H	+ H	$J_{C_2H_6 \longrightarrow C_2H_4+H}$	
C_2H_6	+	$h\nu$	$\longrightarrow$	C_2H_4	+	H_2		$J_{C_2H_6 \longrightarrow C_2H_4+H_2}$	
C_2H_6	+	$h\nu$	$\longrightarrow$	CH_3	+	CH_3		$J_{C_2H_6 \longrightarrow CH_3}$	
C_2H_4	+	$h\nu$	$\longrightarrow$	C_2H_2	+	H_2		$J_{C_2H_4 \longrightarrow H_2}$	Kasting et al. (1983)
C_2H_4	+	$h\nu$	$\longrightarrow$	C_2H_2	+	H	+ H	$J_{C_2H_4 \longrightarrow H}$	
C_2H_2	+	$h\nu$	$\longrightarrow$	C_2H	+	H		$J_{C_2H_2 \longrightarrow C_2H}$	Chen et al. (1991)
C_2H_2	+	$h\nu$	$\longrightarrow$	C_2	+	H_2		$J_{C_2H_2 \longrightarrow C_2}$	and Smith et al. (1991)
CH_2CO	+	$h\nu$	$\longrightarrow$	$^3CH_2$	+	CO		J_{CH_2CO}	Laufer and Keller (1971)
$O(^1D)$			$\xrightarrow{CO_2}$	O				$7.5 \times 10^{-11} e^{\frac{115}{T}}$	Sander et al. (2006)
$O(^1D)$			$\xrightarrow{O_2}$	O				$3.3 \times 10^{-11} e^{\frac{55}{T}}$	Sander et al. (2006)
$O(^1D)$			$\xrightarrow{N_2}$	O				$1.8 \times 10^{-11} e^{\frac{110}{T}}$	Sander et al. (2006)
$^1CH_2$			$\xrightarrow{M}$	$^3CH_2$				8.8×10^{-12}	Ashfold et al. (1981)
O	+	O	$\longrightarrow$	O_2				$2.365 \times 10^{-33} e^{\frac{485}{T}}[M]$	Campbell and Gray (1973)
OH	+	OH	$\longrightarrow$	H_2O	+	O		1.8×10^{-12}	Sander et al. (2006)
OH	+	OH	$\longrightarrow$	H_2O_2				$k_0 = 6.9 \times 10^{-31} \left(\frac{T}{300}\right)^{-1}$	Sander et al. (2003)
								$k_\infty = 2.6 \times 10^{-11}$	
HO_2	+	HO_2	$\longrightarrow$	H_2O_2	+	O_2		$1.5 \times 10^{-12} e^{\frac{19}{T}}$	Christensen et al. (2002)
HO_2	+	HO_2	$\longrightarrow$	H_2O_2	+	O_2		$2.1 \times 10^{-33} e^{\frac{920}{T}}[M]$	Sander et al. (2011)
H	+	H	$\longrightarrow$	H_2				$1.8 \times 10^{-30} \frac{1}{T}[M]$	Baulch et al. (2005)
$^3CH_2$	+	$^3CH_2$	$\longrightarrow$	C_2H_2	+	H_2		5.3×10^{-11}	Banyard et al. (1980) and Laufer (1981)
C_2H_3	+	C_2H_3	$\longrightarrow$	C_2H_4	+	C_2H_2		2.4×10^{-11}	Fahr et al. (1991)
CHO	+	CHO	$\longrightarrow$	CH_2O	+	CO		4.5×10^{-11}	Friedrichs et al. (2002)
CH_3	+	CH_3	$\longrightarrow$	C_2H_6				$k_0 = 1.17 \times 10^{-25} \left(\frac{T}{300}\right)^{-3.75} e^{\frac{-500}{T}}$	Wagner and Wardlaw (1988)
								$k_\infty = 3.0 \times 10^{-11} \left(\frac{T}{300}\right)^{-1}$	and Wang et al. (2003)
O	+	O_2	$\longrightarrow$	O_3				$1.245 \times 10^{-33} \left(\frac{T}{300}\right)^{-2.4}[M]$	Sander et al. (2003)
O	+	O_3	$\longrightarrow$	O_2	+	O_2		$8.0 \times 10^{-12} e^{\frac{-2060}{T}}$	Sander et al. (2003)
$O(^1D)$	+	H_2O	$\longrightarrow$	OH	+	OH		$1.63 \times 10^{-10} e^{\frac{60}{T}}$	Sander et al. (2006)
$O(^1D)$	+	H_2	$\longrightarrow$	OH	+	H		1.2×10^{-10}	Sander et al. (2011)
$O(^1D)$	+	O_3	$\longrightarrow$	O_2	+	O_2		1.2×10^{-10}	Sander et al. (2003)
$O(^1D)$	+	O_3	$\longrightarrow$	O_2	+	O	+ O	1.2×10^{-10}	Sander et al. (2003)
$O(^1D)$	+	CH_4	$\longrightarrow$	CH_3	+	OH		1.125×10^{-10}	Sander et al. (2003)
$O(^1D)$	+	CH_4	$\longrightarrow$	CH_3O	+	H		3.0×10^{-11}	Sander et al. (2003)
$O(^1D)$	+	CH_4	$\longrightarrow$	CH_2O	+	H_2		7.5×10^{-12}	Sander et al. (2003)
O	+	HO_2	$\longrightarrow$	OH	+	O_2		$3.0 \times 10^{-11} e^{\frac{200}{T}}$	Sander et al. (2003)
O	+	OH	$\longrightarrow$	O_2	+	H		$1.8 \times 10^{-11} e^{\frac{180}{T}}$	Sander et al. (2011)
H	+	O_3	$\longrightarrow$	OH	+	O_2		$1.4 \times 10^{-10} e^{\frac{-470}{T}}$	Sander et al. (2003)
H	+	HO_2	$\longrightarrow$	OH	+	OH		7.2×10^{-11}	Sander et al. (2006)
H	+	HO_2	$\longrightarrow$	H_2	+	O_2		6.9×10^{-12}	Sander et al. (2006)
H	+	HO_2	$\longrightarrow$	H_2O	+	O		1.6×10^{-12}	Sander et al. (2006)

Reaction							Rate Coefficient	Reference
OH	+	HO$_2$	$\longrightarrow$	H$_2$O	+	O$_2$	$4.8 \times 10^{-11} e^{\frac{250}{T}}$	Sander et al. (2003)
OH	+	H$_2$O$_2$	$\longrightarrow$	H$_2$O	+	HO$_2$	1.8×10^{-12}	Sander et al. (2006)
OH	+	H$_2$	$\longrightarrow$	H$_2$O	+	H	$2.8 \times 10^{-12} e^{\frac{-1800}{T}}$	Sander et al. (2006)
H	+	O$_2$	$\longrightarrow$	HO$_2$			$k_0 = 4.4 \times 10^{-32} (\frac{T}{300})^{-1.3}$	Sander et al. (2011)
							$k_\infty = 7.5 \times 10^{-11} (\frac{T}{300})^{0.2}$	
O	+	H$_2$O$_2$	$\longrightarrow$	OH	+	HO$_2$	$1.4 \times 10^{-12} e^{\frac{-2000}{T}}$	Sander et al. (2003)
OH	+	O$_3$	$\longrightarrow$	HO$_2$	+	O$_2$	$1.7 \times 10^{-12} e^{\frac{-940}{T}}$	Sander et al. (2003)
HO$_2$	+	O$_3$	$\longrightarrow$	OH	+	O$_2$ + O$_2$	$1.0 \times 10^{-14} e^{\frac{-490}{T}}$	Sander et al. (2003)
CO	+	O	$\longrightarrow$	CO$_2$			$1.625 \times 10^{-32} e^{\frac{-2184}{T}} [M]$	Tsang and Hampson (1986)
CO	+	OH	$\longrightarrow$	CO$_2$	+	H	$k_{1a,0} = 1.34[M] \times 3.62 \times 10^{-26} T^{-2.739} e^{\frac{-20}{T}}$	Joshi and Wang (2006)
							$+[6.48 \times 10^{-33} T^{0.14} e^{\frac{-57}{T}}]^{-1}$	
							$k_{1b,0} = 1.17 \times 10^{-19} T^{2.053} e^{\frac{139}{T}}$	
							$+9.56 \times 10^{-12} T^{-0.664} e^{\frac{-167}{T}}$	
							$k_{1a,\infty} = 1.52 \times 10^{-17} T^{1.858} e^{\frac{28.8}{T}}$	
							$+4.78 \times 10^{-8} T^{-1.851} e^{\frac{-318}{T}}$	
							$F_c = 0.628 e^{\frac{-1223}{T}} + (1 - 0.628) e^{\frac{-39}{T}} + e^{\frac{-T}{255}}$	
C	+	H$_2$	$\longrightarrow$	^{3}CH$_2$			$\dfrac{8.75 \times 10^{-31} e^{\frac{524}{T}} [M]}{1 + \frac{8.75 \times 10^{-31} e^{\frac{524}{T}}}{8.3 \times 10^{-11}} [M]}$	Zahnle (1986)
C	+	O$_2$	$\longrightarrow$	CO	+	O	3.3×10^{-11}	Donovan and Husain (1970)
C	+	OH	$\longrightarrow$	CO	+	H	4.0×10^{-11}	Giguere and Huebner (1978)
C$_2$	+	CH$_4$	$\longrightarrow$	C$_2$H	+	CH$_3$	$5.05 \times 10^{-11} e^{\frac{-297}{T}}$	Pitts et al. (1982)
C$_2$	+	H$_2$	$\longrightarrow$	C$_2$H	+	H	$1.77 \times 10^{-10} e^{\frac{-1469}{T}}$	Pitts et al. (1982)
C$_2$	+	O	$\longrightarrow$	C	+	CO	5.0×10^{-11}	Prasad and Huntress (1980)
C$_2$	+	O$_2$	$\longrightarrow$	CO	+	CO	$1.5 \times 10^{-11} e^{\frac{-550}{T}}$	Baughcum and Oldenborg (1983)
C$_2$H	+	C$_2$H$_2$	$\longrightarrow$	Hcaer	+	H	1.5×10^{-10}	Stephens et al. (1988)
C$_2$H	+	CH$_4$	$\longrightarrow$	C$_2$H$_2$	+	CH$_3$	$6.94 \times 10^{-12} e^{\frac{-250}{T}}$	Lander et al. (1990) and Allen et al. (1992)
C$_2$H	+	H	$\longrightarrow$	C$_2$H$_2$			$\dfrac{1.26 \times 10^{-18} T^{-3.1} e^{\frac{-721}{T}} [M]}{1 + \frac{1.26 \times 10^{-18} T^{-3.1} e^{\frac{-721}{T}}}{3.0 \times 10^{-10}} [M]}$	Tsang and Hampson (1986)
C$_2$H	+	H$_2$	$\longrightarrow$	C$_2$H$_2$	+	H	$5.58 \times 10^{-11} e^{\frac{-1443}{T}}$	Stephens et al. (1988) and Allen et al. (1992)
C$_2$H	+	O	$\longrightarrow$	CO	+	CH	$1.0 \times 10^{-10} e^{\frac{-250}{T}}$	Zahnle (1986)
C$_2$H	+	O$_2$	$\longrightarrow$	CO	+	CHO	2.0×10^{-11}	Brown and Laufer (1982)
C$_2$H$_2$	+	H	$\longrightarrow$	C$_2$H$_3$			$\dfrac{2.6 \times 10^{-31} [M]}{1 + \frac{2.6 \times 10^{-31}}{8.3 \times 10^{-11} e^{\frac{-1374}{T}}} [M]}$	Romani et al. (1993)
C$_2$H$_2$	+	O	$\longrightarrow$	^{3}CH$_2$	+	CO	$2.9 \times 10^{-11} e^{\frac{-1600}{T}}$	Zahnle (1986)
C$_2$H$_2$	+	OH	$\longrightarrow$	CH$_2$CO	+	H	$\dfrac{5.8 \times 10^{-31} e^{\frac{1258}{T}} [M]}{1 + \frac{5.8 \times 10^{-31} e^{\frac{1258}{T}}}{1.4 \times 10^{-12} e^{\frac{388}{T}}} [M]}$	Perry and Williamson (1982)
C$_2$H$_2$	+	OH	$\longrightarrow$	CO	+	CH$_3$	$2.0 \times 10^{-12} e^{\frac{-250}{T}}$	Hampson and Garvin (1977)
C$_2$H$_3$	+	CH$_3$	$\longrightarrow$	C$_2$H$_2$	+	CH$_4$	3.4×10^{-11}	Fahr et al. (1991)
C$_2$H$_3$	+	CH$_4$	$\longrightarrow$	C$_2$H$_4$	+	CH$_3$	$2.4 \times 10^{-24} e^{\frac{-2754}{T}}$	Tsang and Hampson (1986)
C$_2$H$_3$	+	H	$\longrightarrow$	C$_2$H$_2$	+	H$_2$	3.3×10^{-11}	Warnatz (1984)
C$_2$H$_3$	+	H$_2$	$\longrightarrow$	C$_2$H$_4$	+	H	$2.6 \times 10^{-13} e^{\frac{-2646}{T}}$	Allen et al. (1992)
C$_2$H$_3$	+	O	$\longrightarrow$	CH$_2$CO	+	H	5.5×10^{-11}	Hoyermann et al. (1981)
C$_2$H$_3$	+	OH	$\longrightarrow$	C$_2$H$_2$	+	H$_2$O	8.3×10^{-12}	Benson and Haugen (1967)
C$_2$H$_4$	+	O	$\longrightarrow$	CHO	+	CH$_3$	$5.5 \times 10^{-12} e^{\frac{-565}{T}}$	Hampson and Garvin (1977)
C$_2$H$_4$	+	OH	$\longrightarrow$	CH$_2$O	+	CH$_3$	$2.2 \times 10^{-12} e^{\frac{385}{T}}$	Hampson and Garvin (1977)

				Reaction				Rate Coefficient	Reference
CH	+	CO_2	$\longrightarrow$	CHO	+	CO		$5.9 \times 10^{-12} e^{\frac{-350}{T}}$	Berman et al. (1982)
CH	+	H	$\longrightarrow$	C	+	H_2		1.4×10^{-11}	Becker et al. (1989)
CH	+	H_2	$\longrightarrow$	$^3CH_2$	+	H		$2.38 \times 10^{-10} e^{\frac{-1760}{T}}$	Zabarnick et al. (1986)
CH	+	H_2	$\longrightarrow$	CH_3				$\frac{8.75 \times 10^{-31} e^{\frac{524}{T}} [M]}{1 + \frac{8.75 \times 10^{-31} e^{\frac{524}{T}}}{8.3 \times 10^{-11}} [M]}$	Romani et al. (1993)
CH	+	O	$\longrightarrow$	CO	+	H		9.5×10^{-11}	Messing et al. (1981)
CH	+	O_2	$\longrightarrow$	CO	+	OH		5.9×10^{-11}	Butler et al. (1981)
CH	+	CH_4	$\longrightarrow$	C_2H_4	+	H		$\min(2.5 \times 10^{-11} e^{\frac{200}{T}}, 1.7 \times 10^{-10})$	Romani et al. (1993)
$^1CH_2$	+	CH_4	$\longrightarrow$	CH_3	+	CH_3		$7.14 \times 10^{-12} e^{\frac{-5050}{T}}$	Böhland et al. (1985)
$^1CH_2$	+	CO_2	$\longrightarrow$	CH_2O	+	CO		1.0×10^{-12}	Zahnle (1986)
$^1CH_2$	+	H_2	$\longrightarrow$	$^3CH_2$	+	H_2		1.26×10^{-11}	Romani et al. (1993)
$^1CH_2$	+	H_2	$\longrightarrow$	CH_3	+	H		5.0×10^{-15}	Tsang and Hampson (1986)
$^1CH_2$	+	O_2	$\longrightarrow$	CHO	+	OH		3.0×10^{-11}	Ashfold et al. (1981)
$^3CH_2$	+	C_2H_3	$\longrightarrow$	CH_3	+	C_2H_2		3.0×10^{-11}	Tsang and Hampson (1986)
$^3CH_2$	+	CH_3	$\longrightarrow$	C_2H_4	+	H		7.0×10^{-11}	Tsang and Hampson (1986)
$^3CH_2$	+	CO	$\longrightarrow$	CH_2CO				$\frac{1.0 \times 10^{-28} [M]}{1 + \frac{1.0 \times 10^{-28}}{1.0 \times 10^{-15}} [M]}$	Yung et al. (1984)
$^3CH_2$	+	CO_2	$\longrightarrow$	CH_2O	+	CO		1.0×10^{-14}	Darwin and Moore (1995)
$^3CH_2$	+	H	$\longrightarrow$	CH	+	H_2		$4.7 \times 10^{-10} e^{\frac{-370}{T}}$	Zabarnick et al. (1986)
$^3CH_2$	+	H	$\longrightarrow$	CH_3				$\frac{3.1 \times 10^{-30} e^{\frac{475}{T}} [M]}{1 + \frac{3.1 \times 10^{-30} e^{\frac{475}{T}}}{1.5 \times 10^{-10}} [M]}$	Gladstone (1983)
$^3CH_2$	+	O	$\longrightarrow$	CH	+	OH		8.0×10^{-12}	Huebner and Giguere (1980)
$^3CH_2$	+	O	$\longrightarrow$	CO	+	H	+ H	8.3×10^{-11}	Homann and Schweinfurth (1981)
$^3CH_2$	+	O	$\longrightarrow$	CHO	+	H		1.0×10^{-11}	Huebner and Giguere (1980)
$^3CH_2$	+	O_2	$\longrightarrow$	CHO	+	OH		$4.1 \times 10^{-11} e^{\frac{-750}{T}}$	Baulch et al. (1994)
$^3CH_2$	+	C_2H_3	$\longrightarrow$	CH_3	+	C_2H_2		3.0×10^{-11}	Tsang and Hampson (1986)
CH_2CO	+	H	$\longrightarrow$	CH_3	+	CO		$1.9 \times 10^{-11} e^{\frac{-1725}{T}}$	Michael et al. (1979)
CH_2CO	+	O	$\longrightarrow$	CH_2O	+	CO		3.3×10^{-11}	Lee (1980) and Miller et al. (1982)
CH_3	+	CO	$\longrightarrow$	CH_3CO				$1.4 \times 10^{-32} e^{\frac{-3000}{T}} [M]$	Watkins and Word (1974)
CH_3	+	H	$\longrightarrow$	CH_4				$k_0 = 1.0 \times 10^{-28} (\frac{T}{300})^{-1.8}$	Baulch et al. (1994)
								$k_\infty = 2.0 \times 10^{-10} (\frac{T}{300})^{-0.4}$	
CH_3	+	CH_2O	$\longrightarrow$	CH_4	+	CHO		$1.6 \times 10^{-16} (\frac{T}{298})^{6.1} e^{\frac{899}{T}}$	Baulch et al. (1994)
CH_3	+	CHO	$\longrightarrow$	CH_4	+	CO		5.0×10^{-11}	Tsang and Hampson (1986)
CH_3	+	O	$\longrightarrow$	CH_2O	+	H		1.1×10^{-10}	Sander et al. (2006)
CH_3	+	O_2	$\longrightarrow$	CH_2O	+	OH		$k_0 = 4.5 \times 10^{-28} (\frac{T}{300})^{-3.0}$	Sander et al. (2006)
								$k_\infty = 1.8 \times 10^{-12} (\frac{T}{300})^{-1.7}$	
CH_3	+	O_3	$\longrightarrow$	CH_2O	+	HO_2		$5.4 \times 10^{-12} e^{\frac{-220}{T}}$	Sander et al. (2006)
CH_3	+	O_3	$\longrightarrow$	CH_3O	+	O_2		$5.4 \times 10^{-12} e^{\frac{-220}{T}}$	Sander et al. (2006)
CH_3	+	OH	$\longrightarrow$	CH_3O	+	H		$9.3 \times 10^{-11} \frac{T}{298} e^{\frac{-1606}{T}}$	Jasper et al. (2007)
CH_3	+	OH	$\longrightarrow$	CO	+	H_2	+ H_2	6.7×10^{-12}	Fenimore (1969)

Reaction						Rate Coefficient	Reference
CH_3CO	+	CH_3	$\longrightarrow$	C_2H_6	+	CO	5.4×10^{-11}	Adachi et al. (1981)
CH_3CO	+	CH_3	$\longrightarrow$	CH_4	+	CH_2CO	8.6×10^{-11}	Adachi et al. (1981)
CH_3CO	+	H	$\longrightarrow$	CH_4	+	CO	1.0×10^{-10}	Zahnle (1986)
CH_3CO	+	O	$\longrightarrow$	CH_2O	+	CHO	5.0×10^{-11}	Zahnle (1986)
CH_3O	+	CO	$\longrightarrow$	CH_3	+	CO_2	$2.6 \times 10^{-11} e^{\frac{-5940}{T}}$	Wen et al. (1989)
CH_4	+	O	$\longrightarrow$	CH_3	+	OH	$8.75 \times 10^{-12} \left(\frac{T}{298}\right)^{1.5} e^{\frac{-4330}{T}}$	Tsang and Hampson (1986)
CH_4	+	OH	$\longrightarrow$	CH_3	+	H_2O	$2.45 \times 10^{-12} e^{\frac{-1775}{T}}$	Sander et al. (2006)
H	+	CO	$\longrightarrow$	CHO			$1.4 \times 10^{-34} e^{\frac{-1OO}{T}}$ [M]	Baulch et al. (1994)
H	+	CHO	$\longrightarrow$	H_2	+	CO	1.8×10^{-10}	Baulch et al. (1992)
CH_2O	+	H	$\longrightarrow$	H_2	+	CHO	$2.14 \times 10^{-12} \left(\frac{T}{298}\right)^{1.62} e^{\frac{-1090}{T}}$	Baulch et al. (1994)
CH_2O	+	O	$\longrightarrow$	CHO	+	OH	$3.4 \times 10^{-11} e^{\frac{-1600}{T}}$	Sander et al. (2006)
CH_2O	+	OH	$\longrightarrow$	H_2O	+	CHO	$5.5 \times 10^{-12} e^{\frac{125}{T}}$	Sander et al. (2006)
CHO	+	CH_2O	$\longrightarrow$	CH_3O	+	CO	3.8×10^{-17}	Wen et al. (1989)
CHO	+	O_2	$\longrightarrow$	HO_2	+	CO	5.2×10^{-12}	Sander et al. (2006)
O	+	CHO	$\longrightarrow$	H	+	CO_2	5.0×10^{-11}	Tsang and Hampson (1986)
O	+	CHO	$\longrightarrow$	OH	+	CO	1.0×10^{-10}	Hampson and Garvin (1977)
OH	+	CHO	$\longrightarrow$	H_2O	+	CO	1.0×10^{-10}	Tsang and Hampson (1986)

Bilan :

$$CH_4 + 2O_2 \longrightarrow CO_2 + 2H_2O \tag{B1}$$

Tropospheric dominant pathways

$$CH_4 \;+\; OH \;\longrightarrow\; CH_3 \;+\; H_2O$$
$$CH_3 \;+\; O_2 \;\longrightarrow\; CH_2O \;+\; OH$$

CH_2O	+	$h\nu$	$\longrightarrow$	CO	+ H_2
H_2	+	OH	$\longrightarrow$	H_2O	+ H
CO	+	OH	$\longrightarrow$	CO_2	+ H
H	+	O_2	$\longrightarrow$	HO_2	
H	+	O_2	$\longrightarrow$	HO_2	
HO_2	+	HO_2	$\longrightarrow$	H_2O_2	+ O_2
HO_2	+	$h\nu$	$\longrightarrow$	OH	+ OH

CH_2O	+	$h\nu$	$\longrightarrow$	CHO	+ H
CHO	+	O_2	$\longrightarrow$	CO	+ HO_2
CO	+	OH	$\longrightarrow$	CO_2	+ H
H	+	O_2	$\longrightarrow$	HO_2	
H	+	O_2	$\longrightarrow$	HO_2	
HO_2	+	HO_2	$\longrightarrow$	H_2O_2	+ O_2
HO_2	+	$h\nu$	$\longrightarrow$	OH	+ OH
HO_2	+	HO_2	$\longrightarrow$	H_2O_2	+ O_2
H_2O_2	+	OH	$\longrightarrow$	H_2O	+ HO_2

Stratospheric dominant pathway

$$CH_4 + OH \longrightarrow CH_3 + H_2O$$
$$CH_3 + O_2 \longrightarrow CH_2O + OH$$
$$CH_2O + OH \longrightarrow CHO + H_2O$$
$$CHO + O_2 \longrightarrow CO + HO_2$$
$$CO + OH \longrightarrow CO_2 + H$$
$$HO_2 + O \longrightarrow OH + O_2$$
$$H + O_2 \longrightarrow HO_2$$
$$HO_2 + h\nu \longrightarrow OH + O$$
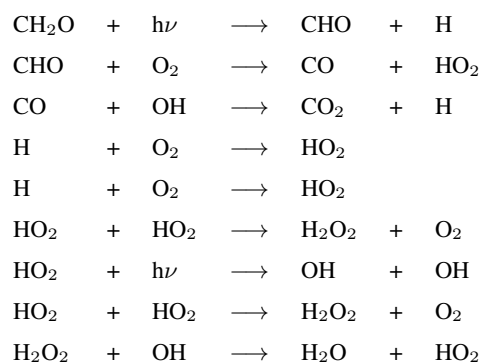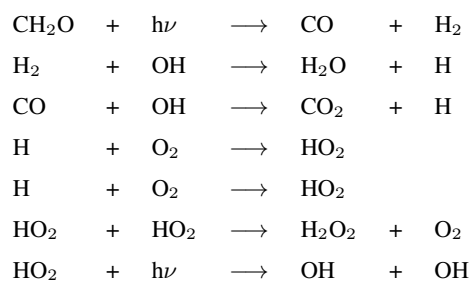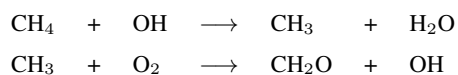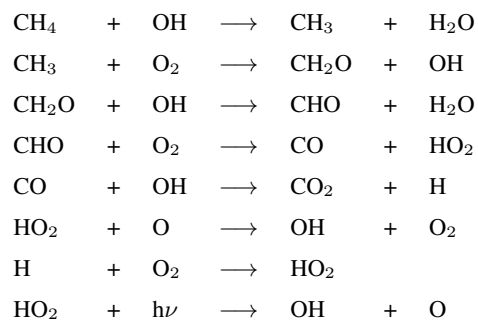
Upper atmosphere dominant pathway

$$CH_4 + h\nu \longrightarrow {}^1CH_2 + H_2$$
$${}^1CH_2 + O_2 \longrightarrow CHO + OH$$
$$CHO + O_2 \longrightarrow CO + HO_2$$
$$CO + OH \longrightarrow CO_2 + H$$
$$HO_2 + O \longrightarrow OH + O_2$$
$$H_2 + O(^1D) \longrightarrow OH + H$$
$$O_2 + h\nu \longrightarrow O + O(^1D)$$
$$H + O_2 \longrightarrow HO_2$$
$$H + O_2 \longrightarrow HO_2$$
$$HO_2 + OH \longrightarrow H_2O + O_2$$
$$HO_2 + OH \longrightarrow H_2O + O_2$$
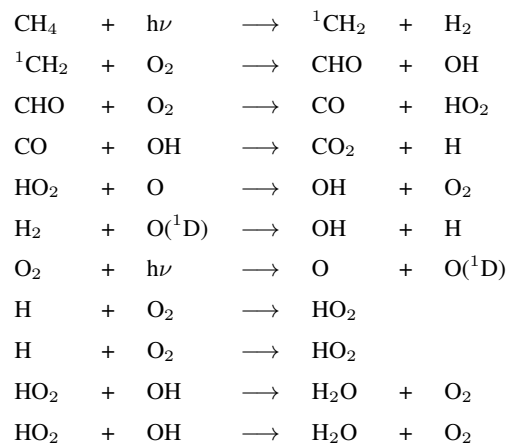
Upper atmosphere secondary pathways (lower half)

$$CH_4 \; + \; h\nu \; \longrightarrow \; CH_3 \; + \; H$$
$$CH_3 \; + \; O_2 \; \longrightarrow \; CH_2O \; + \; OH$$

↙ ↘

CH_2O	+	$h\nu$	$\longrightarrow$	CO	+	H_2	
HO_2	+	O	$\longrightarrow$	OH	+	O_2	
CO	+	OH	$\longrightarrow$	CO_2	+	H	
H_2	+	$O(^1D)$	$\longrightarrow$	OH	+	H	
O_2	+	$h\nu$	$\longrightarrow$	O	+	$O(^1D)$	
H	+	O_2	$\longrightarrow$	HO_2			
H	+	O_2	$\longrightarrow$	HO_2			
H	+	O_2	$\longrightarrow$	HO_2			
HO_2	+	OH	$\longrightarrow$	H_2O	+	O_2	
HO_2	+	OH	$\longrightarrow$	H_2O	+	O_2	

main

CH_2O	+	$h\nu$	$\longrightarrow$	CHO	+	H	
CHO	+	O_2	$\longrightarrow$	CO	+	HO_2	
CO	+	OH	$\longrightarrow$	CO_2	+	H	
HO_2	+	H	$\longrightarrow$	H_2O	+	O	
HO_2	+	O	$\longrightarrow$	OH	+	O_2	
H	+	O_2	$\longrightarrow$	HO_2			
H	+	O_2	$\longrightarrow$	HO_2			
HO_2	+	OH	$\longrightarrow$	H_2O	+	O_2	

$$CH_4 \quad + \quad h\nu \quad \longrightarrow \quad CH_3 \quad + \quad H$$
$$CH_3 \quad + \quad O \quad \longrightarrow \quad CH_2O \quad + \quad H$$

405

$\swarrow$ $\searrow$

CH_2O	+	$h\nu$	$\longrightarrow$	CO	+ H_2
HO_2	+	O	$\longrightarrow$	OH	+ O_2
CO	+	OH	$\longrightarrow$	CO_2	+ H
H_2	+	$O(^1D)$	$\longrightarrow$	OH	+ H
O_2	+	$h\nu$	$\longrightarrow$	O	+ $O(^1D)$
HO_2	+	H	$\longrightarrow$	H_2O	+ O
H	+	O_2	$\longrightarrow$	HO_2	
H	+	O_2	$\longrightarrow$	HO_2	
H	+	O_2	$\longrightarrow$	HO_2	
HO_2	+	OH	$\longrightarrow$	H_2O	+ O_2

CH_2O	+	$h\nu$	$\longrightarrow$	CHO	+ H
CHO	+	O_2	$\longrightarrow$	CO	+ HO_2
CO	+	OH	$\longrightarrow$	CO_2	+ H
HO_2	+	O	$\longrightarrow$	OH	+ O_2
HO_2	+	H	$\longrightarrow$	H_2O	+ O
HO_2	+	H	$\longrightarrow$	H_2O	+ O
H	+	O_2	$\longrightarrow$	HO_2	
H	+	O_2	$\longrightarrow$	HO_2	

main

Author contributions. Adam Yassin Jaziri participate to the conceptualization, investigation and methodology. Benjamin Charnay coordinate the porject and participate to the conceptualization, supervision and validation. Franck Selsis participate to the supervision and the validation. Jérémy Leconte provide the funding acquisition, resources, participate to the software check up and the validation. Franck Lefèvre and Adam Yassin Jaziri developped the part of the software needed for this work. Adam Yassin Jaziri made the visualization and write the original draft

410 while Benjamin Charnay, Franck Selsis, Jérémy Leconte and Franck Lefèvre participate to the review and editing process.

Competing interests. The authors declare that they have no conflict of interest.

Acknowledgements. This project has received funding from the European Research Council (ERC) under the European Union's Horizon 2020 research and innovation programme (grant agreement No. 679030/WHIPLASH).

References

Adachi, H., Basco, N., and James, D.: The acetyl radicals CH3CO· and CD3CO· studied by flash photolysis and kinetic spectroscopy, International Journal of Chemical Kinetics, 13, 1251 – 1276, https://doi.org/10.1002/kin.550131206, 1981.

Allen, M., Yung, Y., and Gladstone, G.: The relative abundance of ethane to acetylene in the Jovian stratosphere, Icarus, 100, 527–33, https://doi.org/10.1016/0019-1035(92)90115-N, 1992.

Arney, G., Domagal-Goldman, S., Meadows, V., Wolf, E., Schwieterman, E., Charnay, B., Claire, M., Hébrard, E., and G. Trainer, M.: The Pale Orange Dot: The Spectrum and Habitability of Hazy Archean Earth, Astrobiology, 16, https://doi.org/10.1089/ast.2015.1422, 2016.

Ashfold, M., Fullstone, M., Hancock, G., and Ketley, G.: Singlet methylene kinetics, Chemical Physics, 55, 245–257, https://doi.org/10.1016/0301-0104(81)85026-4, 1981.

Awramik, S., Schopf, J., and Walter, M.: Filamentous fossil bacteria from the Archean of Western Australia, in: Developments in Precambrian Geology, vol. 7, pp. 249–266, Elsevier, 1983.

Bachan, A. and Kump, L. R.: The rise of oxygen and siderite oxidation during the Lomagundi Event, Proceedings of the National Academy of Sciences, 112, 6562–6567, 2015.

Banyard, S., Canosa-Mas, C., Ellis, M., Frey, H., and Walsh, R.: Keten photochemistry. Some observations on the reactions and reactivity of triplet methylene, Journal of The Chemical Society, Chemical Communications, https://doi.org/10.1039/c39800001156, 1980.

Bartlett, B. C. and Stevenson, D. J.: Analysis of a Precambrian resonance-stabilized day length, Geophysical Research Letters, 43, 5716–5724, 2016.

Baughcum, S. and Oldenborg, R.: Measurement of the C2($a^3 \prod_u$) and C2($X^1 \sum_g^+$) Disappearance Rates with O2 from 298 to 1300 Kelvin, pp. 257–266, https://doi.org/10.1021/bk-1983-0249.ch015, 1983.

Baulch, D., Cobos, C., Cox, R., Esser, C., Frank, P., Just, T., Kerr, J., Pilling, M., Troe, J., Warnatz, J., and Walker, R.: Evaluated Kinetic Data for Combustion Modeling, J.Phys.Chem.Ref.Data 21 (1992) 3, pp. 411-734, 21, https://doi.org/10.1063/1.555908, 1992.

Baulch, D., Cobos, C., Cox, R., Esser, C., Frank, P., Just, T., Kerr, J., Pilling, M., Troe, J., Walker, R., and Warnatz, J.: Evaluated kinetic data for combustion modelling, pp. 111–125, 1994.

Baulch, D., Bowman, C., Cobos, C., Cox, R., Just, T., Kerr, J., Pilling, M., Stocker, D., Troe, J., Tsang, W., Walker, R., and Warnatz, J.: Evaluated Kinetic Data for Combustion Modeling: Supplement II, Journal of Physical and Chemical Reference Data, 34, https://doi.org/10.1063/1.1748524, 2005.

Becker, K., Engelhardt, B., Wiesen, P., and Bayes, K.: Rate constants for CH($X^2 \prod$) reactions at low total pressures, Chemical Physics Letters, 154, 342–348, https://doi.org/10.1016/0009-2614(89)85367-9, 1989.

Benson, S. W. and Haugen, G. R.: The mechanism of the high temperature reaction of atomic hydrogen with acetylene over an extended pressure and temperature range, J. Chem. Phys., 71, 4404–4411, 1967.

Berman, M., Fleming, J., Harvey, A., and Lin, M.: Temperature dependence of CH radical reactions with O2, NO, CO and CO2, Symposium (International) on Combustion, 19, https://doi.org/10.1016/S0082-0784(82)80179-3, 1982.

Böhland, T., Dõbẽ, S., Temps, F., and Wagner, H. G.: Kinetics of the Reactions between CH2($X^3B_1$1)-Radicals and Saturated Hydrocarbons in the Temperature Range 296 K $\leq$ T $\leq$ 707 K, Berichte der Bunsengesellschaft für physikalische Chemie, 89, 1110 – 1116, https://doi.org/10.1002/bbpc.19850891018, 1985.

Bolmont, E., Libert, A.-S., Leconte, J., and Selsis, F.: Habitability of planets on eccentric orbits: the limits of the mean flux approximation, Astronomy Astrophysics, 591, https://doi.org/10.1051/0004-6361/201628073, 2016.

Bowring, S. A. and Williams, I. S.: Priscoan (4.00–4.03 Ga) orthogneisses from northwestern Canada, Contributions to Mineralogy and Petrology, 134, 3–16, 1999.

Brasier, M., McLoughlin, N., Green, O., and Wacey, D.: A fresh look at the fossil evidence for early Archaean cellular life, Philosophical Transactions of the Royal Society B: Biological Sciences, 361, 887–902, 2006.

455 Brown, R. and Laufer, A.: Calculation of activation energies for hydrogen-atom abstractions by radicals containing carbon triple bonds, The Journal of Physical Chemistry, 85, https://doi.org/10.1021/j150625a022, 1982.

Butler, J., Fleming, J., Goss, L., and Lin, M.: Kinetics of CH radical reactions with selected molecules at room temperature, Chemical Physics, 56, 355–365, https://doi.org/10.1016/0301-0104(81)80157-7, 1981.

Cadeau, P., Jézéquel, D., Leboulanger, C., Fouilland, É., Le Floc'h, E., Chaduteau, C., Milesi, V., Guélard, J., Sarazin, G., Katz, A., et al.:
460   Carbon isotope evidence for large methane emissions to the Proterozoic atmosphere, Scientific reports, 10, 1–13, 2020.

Campbell, I. and Gray, C.: Rate constants for O(3P) recombination and association with N(4S), Chemical Physics Letters, 18, 607–609, https://doi.org/10.1016/0009-2614(73)80479-8, 1973.

Catling, D. and Zahnle, K.: The Archean atmosphere, Science Advances, 6, eaax1420, https://doi.org/10.1126/sciadv.aax1420, 2020.

Catling, D., Zahnle, K., and McKay, C.: Biogenic Methane, Hydrogen Escape, and the Irreversible Oxidation of Early Earth, Science (New
465   York, N.Y.), 293, 839–43, https://doi.org/10.1126/science.1061976, 2001.

Chan, W., Cooper, G., and Brion, C.: The electronic spectrum of carbon dioxide. Discrete and continuum photoabsorption oscillator strengths (6–203 eV), Chemical Physics, 178, 401–413, https://doi.org/10.1016/0301-0104(93)85079-N, 1993.

Charnay, B., Forget, F., Wordsworth, R., Leconte, J., Millour, E., Codron, F., and Spiga, A.: Exploring the faint young Sun problem and the possible climates of the Archean Earth with a 3-D GCM, Journal of Geophysical Research: Atmospheres, 118,
470   https://doi.org/10.1002/jgrd.50808, 2013.

Charnay, B., Wolf, E. T., Marty, B., and Forget, F.: Is the faint young Sun problem for Earth solved?, Space Science Reviews, 216, 1–29, 2020.

Chen, F. and Wu, C.: Temperature-dependent photoabsorption cross sections in the VUV-UV region. I. Methane and ethane, Journal of Quantitative Spectroscopy and Radiative Transfer, 85, 195–209, https://doi.org/10.1016/S0022-4073(03)00225-5, 2004.

475 Chen, F., Judge, D. L., Robert Wu, C. Y., Caldwell, J., White, H. P., and Wagener, R.: High-resolution, low-temperature photoabsorption cross sections of C2H2, PH3, AsH3, and GeH4, with application to Saturn's atmosphere, Journal of Geophysical Research: Planets, 96, 17 519–17 527, https://doi.org/10.1029/91JE01687, 1991.

Christensen, L., Okumura, M., Sander, S., Salawitch, R., Toon, G., CSen, B., Blavier, J.-F., and Jucks, K.: Kinetics of HO2 + HO2 $\longrightarrow$ H2O2 + O2: Implications for stratospheric H2O2, Geophysical Research Letters, 29, https://doi.org/10.1029/2001GL014525, 2002.

480 Chung, C.-Y., Chew, E. P., Cheng, B.-M., Bahou, M., and Lee, Y.-P.: Temperature dependence of absorption cross-section of H2O, HOD, and D2O in the spectral region 140–193nm, Nuclear Instruments and Methods in Physics Research Section A: Accelerators, Spectrometers, Detectors and Associated Equipment, 467-468, 1572–1576, https://doi.org/10.1016/S0168-9002(01)00762-8, 2001.

Claire, M., C. CATLING, D., and J. ZAHNLE, K.: Biogeochemical modelling of the rise in atmospheric oxygen, Geobiology, 4, 239 – 269, https://doi.org/10.1111/j.1472-4669.2006.00084.x, 2006.

485 Claire, M., Sheets, J., Meadows, V., Cohen, M., Ribas, I., and Catling, D.: The evolution of solar flux from 0.1 nm to 160 μm: Quantitative estimates for planetary studies, Astrophysical Journal, 757, https://doi.org/10.1088/0004-637X/757/1/95, 2012.

Crowe, S. A., DOssing, L. N., Beukes, N. J., Bau, M., Kruger, S. J., Frei, R., and Canfield, D. E.: Atmospheric oxygenation three billion years ago, Nature, 501, 535–538, 2013.

D. Wordsworth, R., Forget, F., Millour, E., Head, J., Madeleine, J.-B., and Charnay, B.: Global modelling of the early Martian climate under a denser CO2 atmosphere: Water cycle and ice evolution, Icarus, 222, https://doi.org/10.1016/j.icarus.2012.09.036, 2012.

Darwin, D. and Moore, C.: Reaction Rate Constants (295 K) for 3CH2 with H2S, SO2, and NO2: Upper Bounds for Rate Constants with Less Reactive Partners, The Journal of Physical Chemistry, 99, 13 467–13 470, https://doi.org/10.1021/j100036a022, 1995.

Demore, W., Sander, S., Golden, D., Hampson, R., Kurylo, M., Howard, C., Ravishankara, A., Kolb, C., and Molina, M.: Chemical Kinetics and Photochemical Data for Use in Stratospheric Modeling, JPL Publication, 90, 1997.

Donovan, R. and Husain, D.: Recent advances in the chemistry of electronically excited atoms, Chemical Reviews, 70, https://doi.org/10.1021/cr60266a003, 1970.

Fahr, A., Laufer, A., Klein, R., and Braun, W.: Reaction Rate Determinations of Vinyl Radical Reactions with Vinyl, Methyl, and Hydrogen Atoms, The Journal of Physical Chemistry, 95, https://doi.org/10.1021/j100161a047, 1991.

Fally, S., Vandaele, A., Carleer, M., Hermans, C., Jenouvrier, A., Merienne, M.-F., Coquart, B., and Colin, R.: Fourier Transform Spectroscopy of the O2 Herzberg Bands. III. Absorption Cross Sections of the Collision-Induced Bands and of the Herzberg Continuum, Journal of Molecular Spectroscopy, 204, 10–20, https://doi.org/10.1006/jmsp.2000.8204, 2000.

Farquhar, J., Peters, M., Johnston, D., Strauss, H., Masterson, A., Wiechert, U., and Kaufman, A.: Isotopic evidence for Mesoarchaean anoxia and changing atmospheric sulphur chemistry, Nature, 449, 706–9, https://doi.org/10.1038/nature06202, 2007.

Fauchez, T., Turbet, M., Villanueva, G., Wolf, E., Arney, G., Kopparapu, R., Lincowski, A., Mandell, A., De Wit, J., Pidhorodetska, D., Domagal-Goldman, S., and Stevenson, K.: Impact of Clouds and Hazes on the Simulated JWST Transmission Spectra of Habitable Zone Planets in the TRAPPIST-1 System, 2019.

Fenimore, C.: Destruction of methane in water gas by reaction of CH3 with OH radicals, Symposium (international) on Combustion, 12, 463–467, https://doi.org/10.1016/S0082-0784(69)80428-5, 1969.

Forget, F., Wordsworth, R., Millour, E., Madeleine, J.-B., Kerber, L., Leconte, J., Marcq, E., and M. Haberle, R.: 3D modelling of the early Martian climate under a denser CO2 atmosphere: Temperatures and CO2 ice clouds, Icarus, 222, https://doi.org/10.1016/j.icarus.2012.10.019, 2012.

Friedrichs, G., Herbon, J., Davidson, D., and Hanson, R.: Quantitative detection of HCO behind shock waves: The thermal decomposition of HCO, Physical Chemistry Chemical Physics, 4, 5778–5788, https://doi.org/10.1039/b205692e, 2002.

Furnes, H., Banerjee, N. R., Muehlenbachs, K., Staudigel, H., and de Wit, M.: Early life recorded in Archean pillow lavas, Science, 304, 578–581, 2004.

Gaillard, F., Scaillet, B., and Arndt, N.: Atmospheric oxygenation caused by a change in volcanic degassing pressure, Nature, 478, 229–32, https://doi.org/10.1038/nature10460, 2011.

Gebauer, S., Grenfell, J., Stock, J., Lehmann, R., Godolt, M., Von Paris, P., and Rauer, H.: Evolution of Earth-like extrasolar planetary atmospheres: Assessing the atmospheres and biospheres of early Earth analog planets with a coupled atmosphere biogeochemical model, Astrobiology, 17, 2017.

Gebauer, S., Grenfell, J., Lehmann, R., and Rauer, H.: Evolution of Earth-like Planetary Atmospheres around M Dwarf Stars: Assessing the Atmospheres and Biospheres with a Coupled Atmosphere Biogeochemical Model, Astrobiology, 18, 856–872, https://doi.org/10.1089/ast.2017.1723, 2018.

Gibson, S., Gies, H., Blake, A., McCoy, D., and Rogers, P.: Temperature dependence in the Schumann-Runge photoabsorption continuum of oxygen, Journal of Quantitative Spectroscopy and Radiative Transfer, 30, 385–393, https://doi.org/10.1016/0022-4073(83)90101-2, 1983.

Giguere, P. and Huebner, W.: A model of comet comae. I - Gas-phase chemistry in one dimension, The Astrophysical Journal, 223, 638–654, https://doi.org/10.1086/156298, 1978.

Gladstone, G.: Radiative transfer and photochemistry in the upper atmosphere of Jupiter, Calif. Inst. of Technol., Pasaden, p. Ph.D. thesis, 1983.

530   Goldblatt, C., M Lenton, T., and Watson, A.: Bistability of atmospheric oxygen and the Great Oxidation, Nature, 443, 683–6, https://doi.org/10.1038/nature05169, 2006.

Gregory, B. S., Claire, M. W., and Rugheimer, S.: Photochemical modelling of atmospheric oxygen levels confirms two stable states, Earth and Planetary Science Letters, 561, 116 818, 2021.

Hampson and Garvin, D.: Reaction Rate and Photochemical Data for Atmospheric Chemistry, Natl. Bur. Stand. Spec. Publ. No. 513, 1977.

535   Haqq-Misra, J. D., Domagal-Goldman, S. D., Kasting, P. J., and Kasting, J. F.: A revised, hazy methane greenhouse for the Archean Earth, Astrobiology, 8, 1127–1137, 2008.

Harada, M., Tajika, E., and Sekine, Y.: Transition to an oxygen-rich atmosphere with an extensive overshoot triggered by the Paleoproterozoic snowball Earth, Earth and Planetary Science Letters, 419, https://doi.org/10.1016/j.epsl.2015.03.005, 2015.

Hodgskiss, M., Crockford, P., Peng, Y., Wing, B., Horner, T., and Thiemens, M.: A Productivity Collapse to end Earth's Great Oxidation,
540   Proceedings of the National Academy of Sciences, 116, https://doi.org/10.1073/pnas.1900325116, 2019.

Holland, H. and Bekker, A.: Oxygen Overshoot and Recovery during the Paleoproterozoic, Earth and Planetary Science Letters, s 317-318, https://doi.org/10.1016/j.epsl.2011.12.012, 2012.

Homann, K. and Schweinfurth, H.: Kinetics and Mechanism of Hydrocarbon Formation in the System C2H2/H, Berichte der Bunsenge-sellschaft für physikalische Chemie, 85, 569 – 577, https://doi.org/10.1002/bbpc.19810850710, 1981.

545   Hoyermann, K., Loftfield, N., Sievert, R., and Wagner, H.: Mechanisms and rates of the reactions of CH3O and CH2OH radicals with H atoms, Symposium (International) on Combustion, 18, 831–842, https://doi.org/10.1016/S0082-0784(81)80086-0, 1981.

Huebner, W. and Giguere, P.: A model of comet comae. II - Effects of solar photodissociative ionization, Astrophys. J., 238, https://doi.org/10.1086/158033, 1980.

Jasper, A., Klippenstein, S., Harding, L., and Ruscic, B.: Kinetics of the Reaction of Methyl Radical with Hydroxyl Radical and Methanol
550   Decomposition †, The journal of physical chemistry. A, 111, 3932–50, https://doi.org/10.1021/jp067585p, 2007.

Joshi, A. and Wang, H.: Master equation modeling of wide range temperature and pressure dependence of CO + OH ⟶ products, International Journal of Chemical Kinetics, 38, 57 – 73, https://doi.org/10.1002/kin.20137, 2006.

Kameta, K., Kouchi, N., Ukai, M., and Hatano, Y.: Photoabsorption, photoionization, and neutral-dissociation cross sections of simple hydrocarbons in the vacuum ultraviolet range, Journal of Electron Spectroscopy and Related Phenomena, 123, 225–238,
555   https://doi.org/10.1016/S0368-2048(02)00022-1, 2002.

Kasting, J., Zahnle, K., and Walker, J.: Photochemistry of methane in the Earth's early atmosphere, Precambrian Research, 20, 121–148, https://doi.org/10.1016/0301-9268(83)90069-4, development and interactions of the Precambrian atmosphere, lithosphere and biosphere: results and challenges, 1983.

Kasting, J., Zahnle, K., Pinto, J., and Young, A.: Sulfur, ultraviolet radiation, and the early evolution of life, Origins of life and evolution of
560   the biosphere, 19, 252–253, https://doi.org/10.1007/BF02388836, 1989.

Lander, D., Unfried, K., Glass, G., and Curl, R.: Rate constant measurements of C2H with CH4, C2H6, C2H4, D2, and CO, Journal of Physical Chemistry, 94, 7759–7763, 1990.

Laufer, A.: Kinetics of gas phase reactions of methylene, Reviews of Chemical Intermediates, 4, 225–257, https://doi.org/10.1007/BF03052416, 1981.

565 Laufer, A. and Keller, R.: Lowest excited states of ketene, Journal of The American Chemical Society, 93, https://doi.org/10.1021/ja00730a010, 1971.

Leconte, J., Forget, F., Charnay, B., Wordsworth, R., Selsis, F., Millour, E., and Spiga, A.: 3D climate modeling of close-in land planets: Circulation patterns, climate moist bistability and habitability, Astronomy and Astrophysics, 554, 69–, https://doi.org/10.1051/0004-6361/201321042, 2013.

570 Lee, A., Yung, Y., Cheng, B.-M., Bahou, M., Chung, C.-Y., and Lee, a.: Enhancement of Deuterated Ethane on Jupiter, The Astrophysical Journal Letters, 551, L93, https://doi.org/10.1086/319827, 2001.

Lee, L.: CN($A^2\prod_i \longrightarrow X^2\sum^+$) and CN($B^2\sum^+ \longrightarrow X^2\sum^+$) yields from HCN photodissociation, The Journal of Chemical Physics, 72, https://doi.org/10.1063/1.439140, 1980.

Lefèvre, F., Figarol, F., Carslaw, K. S., and Peter, T.: The 1997 Arctic ozone depletion quantified from three-dimensional model simulations,
575 Geophysical research letters, 25, 2425–2428, 1998.

Lefèvre, F., Lebonnois, S., Montmessin, F., and Forget, F.: Three-dimensional modeling of ozone on Mars, Journal of Geophysical Research, 109, https://doi.org/10.1029/2004JE002268, 2004.

Lewis, B. and Carver, J.: Temperature dependence of the carbon dioxide photoabsorption cross section between 1200 and 1970 Å, Journal of Quantitative Spectroscopy and Radiative Transfer, 30, 297–309, https://doi.org/10.1016/0022-4073(83)90027-4, 1983.

580 Lewis, B. R., Vardavas, I. M., and Carver, J. H.: The aeronomic dissociation of water vapor by solar H Lyman α radiation, Journal of Geophysical Research: Space Physics, 88, 4935–4940, https://doi.org/10.1029/JA088iA06p04935, 1983.

Lowe, D. R. and Tice, M. M.: Geologic evidence for Archean atmospheric and climatic evolution: Fluctuating levels of CO2, CH4, and O2 with an overriding tectonic control, Geology, 32, 493–496, 2004.

Lyons, T., Reinhard, C., and J Planavsky, N.: The rise of oxygen in Earth's early ocean and atmosphere, Nature, 506, 307–315,
585 https://doi.org/10.1038/nature13068, 2014.

Messing, I., Filseth, S., Sadowski, C., and Carrington, T.: Absolute rate constants for the reactions of CH with O and N atoms, The Journal of Chemical Physics, 74, https://doi.org/10.1063/1.441563, 1981.

Michael, J., Nava, D., Payne, W., and Stief, L.: Absolute rate constants for the reaction of atomic hydrogen with ketene from 298 to 500 K, The Journal of Chemical Physics, 70, https://doi.org/10.1063/1.437314, 1979.

590 Miller, J., Mitchell, R., and Smooke, M.: Toward a Comprehensive Chemical Kinetic Mechanism for the Oxidation of Acetylene: Comparison of Model Predictions with Results from Flame and Shock Tube Experiments, Symposium (International) on Combustion, 19, 181–196, https://doi.org/10.1016/S0082-0784(82)80189-6, 1982.

Minschwaner, K., Anderson, G. P., Hall, L. A., and Yoshino, K.: Polynomial coefficients for calculating O2 Schumann-Runge cross sections at 0.5 cm-1 resolution, Journal of Geophysical Research: Atmospheres, 97, 10 103–10 108, https://doi.org/10.1029/92JD00661, 1992.

595 Mota, R., Parafita, R., Giuliani, A., Hubin-Franskin, M.-J., Lourenco, J., Garcia, G., Hoffmann, S., Mason, N., Ribeiro, P., Raposo, M., and Limao-Vieira, P.: Water VUV electronic state spectroscopy by synchrotron radiation, Chemical Physics Letters, 416, 152–159, https://doi.org/10.1016/j.cplett.2005.09.073, 2005.

Nisbet, E., Grassineau, N., Howe, C., Abell, P., Regelous, M., and Nisbet, R.: The age of Rubisco: the evolution of oxygenic photosynthesis, Geobiology, 5, 311–335, 2007.

600 Ogawa, S. and Ogawa, M.: Absorption Cross Sections of O2($a^1\Delta_g$) and O2($X^3\sum_g^-$) in the Region from 1087 to 1700 A, Canadian Journal of Physics, 53, 1845–1852, https://doi.org/10.1139/p75-236, 1975.

Parkinson, W., Rufus, J., and Yoshino, K.: Absolute absorption cross section measurements of CO2 in the wavelength region 163-200 nm and the temperature dependence, Chemical Physics, 290, 251–256, https://doi.org/10.1016/S0301-0104(03)00146-0, 2003.

Partin, C. A., Bekker, A., Planavsky, N. J., Scott, C., Gill, B. C., Li, C., Podkovyrov, V., Maslov, A., Konhauser, K. O., Lalonde, S. V.,
605 et al.: Large-scale fluctuations in Precambrian atmospheric and oceanic oxygen levels from the record of U in shales, Earth and Planetary Science Letters, 369, 284–293, 2013.

Pavlov, A. and Kasting, J.: Mass-independent fractionation of sulfur isotopes in Archean sediments: strong evidence for an anoxic Archean atmosphere, Astrobiology, 2, 27–41, 2002.

Pavlov, A., Brown, L., and Kasting, J.: UV shielding of NH3 and O2 by organic hazes in the Archean atmosphere, Journal of Geophysical
610 Research, 106, 23 267–23 288, https://doi.org/10.1029/2000JE001448, 2001.

Perry, R. and Williamson, D.: Pressure and temperature dependence of the OH radical reaction with acetylene, Chemical Physics Letters, 93, 331–334, https://doi.org/10.1016/0009-2614(82)83703-2, 1982.

Pierrehumbert, R. T.: Principles of Planetary Climate, Cambridge University Press, https://doi.org/10.1017/CBO9780511780783, 2010.

Pitts, W. M., Pasternack, L., and McDonald, J.: Temperature dependence of the C2($X^1\sum_g^+$) reaction with H2 and CH4 and C2($X^1\sum_g^+$ and
615 $a^3\prod_u$ equilibrated states) with O2, Chemical Physics, 68, 417–422, https://doi.org/10.1016/0301-0104(82)87050-X, 1982.

Planavsky, N. J., Bekker, A., Hofmann, A., Owens, J. D., and Lyons, T. W.: Sulfur record of rising and falling marine oxygen and sulfate levels during the Lomagundi event, Proceedings of the National Academy of Sciences, 109, 18 300–18 305, 2012.

Planavsky, N. J., Asael, D., Hofmann, A., Reinhard, C. T., Lalonde, S. V., Knudsen, A., Wang, X., Ossa, F. O., Pecoits, E., Smith, A. J., et al.: Evidence for oxygenic photosynthesis half a billion years before the Great Oxidation Event, Nature Geoscience, 7, 283–286, 2014.

620 Prasad, S. and Huntress, W.: A Model for Gas Phase Chemistry in Interstellar Clouds. II - Nonequilibrium Effects and Effects of Temperature and Activation Energies, The Astrophysical Journal, 239, https://doi.org/10.1086/158097, 1980.

Romani, P., Bishop, J., Bezard, B., and Atreya, S.: Methane Photochemistry on Neptune: Ethane and Acetylene Mixing Ratios and Haze Production, Icarus, 106, https://doi.org/10.1006/icar.1993.1184, 1993.

Sander, S., Friedl, R., Golden, D., Kurylo, M., Huie, R., Orkin, V., Moortgat, G., Ravishankara, A., Kolb, C., Molina, M., and Finlayson-Pitts,
625 B.: Chemical Kinetics and Photochemical Data for Use in Atmosheric Studies; JPL Publication 02-25, 2003.

Sander, S., Finlayson-Pitts, B., Friedl, R., Golden, D., Huie, R., Keller-Rudek, H., Kolb, C., Kurylo, M., Molina, M., Moortgat, G., Orkin, V., Ravishankara, A., and Wine, P.: Chemical Kinetics and Photochemical Data for Use in Atmospheric Studies. Evaluation No. 15 (JPL Publication 06-2), 2006.

Sander, S., Abbatt, J., Barker, J., Burkholder, J., Friedl, R., Golden, D., Huie, R., Kurylo, M., Moortgat, G., Orkin, V., and Wine, P.: Chemical
630 Kinetics and Photochemical Data for Use in Atmospheric Studies, Evaluation No. 17, 2011.

Satkoski, A. M., Beukes, N. J., Li, W., Beard, B. L., and Johnson, C. M.: A redox-stratified ocean 3.2 billion years ago, Earth and Planetary Science Letters, 430, 43–53, 2015.

Sauterey, B., Charnay, B., Affholder, A., Mazevet, S., and Ferrière, R.: Co-evolution of primitive methane-cycling ecosystems and early Earth's atmosphere and climate, Nature Communications, 11, 1234567 890, https://doi.org/10.1038/s41467-020-16374-7, 2020.

635 Schirrmeister, B. E., Sanchez-Baracaldo, P., and Wacey, D.: Cyanobacterial evolution during the Precambrian, International Journal of Astrobiology, 15, 187–204, 2016.

Schröder, S., Bekker, A., Beukes, N., Strauss, H., and Van Niekerk, H.: Rise in seawater sulphate concentration associated with the Paleo-proterozoic positive carbon isotope excursion: evidence from sulphate evaporites in the 2.2–2.1 Gyr shallow-marine Lucknow Formation, South Africa, Terra Nova, 20, 108–117, 2008.

640 Schurgers, M. and Welge, K. H.: Absorptionskoeffizient von H2O2 und N2H4 zwischen 1200 und 2000 A, Zeitschrift fur Naturforschung A, 23, 1508–1510, https://doi.org/doi:10.1515/zna-1968-1011, 1968.

Selsis, F., Wordsworth, R., and Forget, F.: Thermal phase curves of nontransiting terrestrial exoplanets I. Characterizing atmospheres, Astronomy Astrophysics - ASTRON ASTROPHYS, 532, https://doi.org/10.1051/0004-6361/201116654, 2011.

Smith, P., Yoshino, K., Parkinson, W., Ito, K., and Stark, G.: High-resolution, VUV (147-201 nm) photoabsorption cross sections for C2H2

645 at 195 and 295 K, Journal of Geophysical Research Atmospheres, 96, https://doi.org/10.1029/91JE01739, 1991.

Stark, G., Yoshino, K., Smith, P., and Ito, K.: Photoabsorption cross section measurements of CO2 between 106.1 and 118.7nm at 295 and 195K, Journal of Quantitative Spectroscopy and Radiative Transfer, 103, 67–73, https://doi.org/10.1016/j.jqsrt.2006.07.001, 2007.

Stephens, J., Hall, J., Solka, H., Yan, W.-B., Curl, R., and Glass, G.: ChemInform Abstract: Rate Constant Measurements of Reactions of C2H with H2, O2, C2H2, and NO Using Color Center Laser Kinetic Spectroscopy, ChemInform, 19, https://doi.org/10.1002/chin.198806109,

650 1988.

Thompson, B. A., Harteck, P., and Reeves Jr., R. R.: Ultraviolet absorption coefficients of CO2, CO, O2, H2O, N2O, NH3, NO, SO2, and CH4 between 1850 and 4000 A, Journal of Geophysical Research (1896-1977), 68, 6431–6436, https://doi.org/10.1029/JZ068i024p06431, 1963.

Tian, W., Chipperfield, M. P., Stevenson, D. S., Damoah, R., Dhomse, S., Dudhia, A., Pumphrey, H., and Bernath, P.: Effects of stratosphere-

655 troposphere chemistry coupling on tropospheric ozone, Journal of Geophysical Research: Atmospheres, 115, 2010.

Tsang, W. and Hampson, R.: Chemical Kinetic Data Base for Combustion Chemistry. Part I. Methane and Related Compounds, Journal of Physical and Chemical Reference Data, 15, 1087–1279, https://doi.org/10.1063/1.555759, 1986.

Turbet, M., Bolmont, E., Ehrenreich, D., Gratier, P., Leconte, J., Selsis, F., Hara, N., and Lovis, C.: Revised mass-radius relationships for water-rich rocky planets more irradiated than the runaway greenhouse limit, Astronomy Astrophysics, 638, https://doi.org/10.1051/0004-

660 6361/201937151, 2020a.

Turbet, M., Boulet, C., and Karman, T.: Measurements and semi-empirical calculations of CO2 + CH4 and CO2 + H2 collision-induced absorption across a wide range of wavelengths and temperatures. Application for the prediction of early Mars surface temperature, Icarus, 346, 113 762, https://doi.org/10.1016/j.icarus.2020.113762, 2020b.

Vinson, A. M. and Hansen, B. M.: On the spin states of habitable zone exoplanets around M dwarfs: the effect of a near-resonant companion,

665 Monthly Notices of the Royal Astronomical Society, 472, 3217–3229, 2017.

Wagner, A. F. and Wardlaw, D. M.: Study of the recombination reaction CH3 + CH3 = C2H6, Theory, J. Phys. Chem., 92, 2462–2471, 1988.

Wang, B., Hou, H., Yoder, L., Muckerman, J., and Fockenberg, C.: Experimental and Theoretical Investigations on the Methyl-Methyl Recombination Reaction, Journal of Physical Chemistry A, 107, https://doi.org/10.1021/jp030657h, 2003.

Warnatz, J.: Rate Coefficients in the C/H/O System, pp. 197–360, https://doi.org/10.1007/978-1-4684-0186-8_5, 1984.

670 Watkins, K. and Word, W.: Addition of methyl radicals to carbon monoxide: Chemically and thermally activated decomposition of acetyl radicals, International Journal of Chemical Kinetics, 6, 855 – 873, https://doi.org/10.1002/kin.550060608, 1974.

Wen, J.-S., Pinto, J., and Yung, Y.: Photochemistry of CO and H2O: Analysis of Laboratory Experiments and Applications to the Prebiotic Earth's Atmosphere, Journal of Geophysical Research D, 94, 1989.

Yoshino, K., Cheung, A.-C., Esmond, J., Parkinson, W., Freeman, D., Guberman, S., Jenouvrier, A., Coquart, B., and Merienne, M.: Improved absorption cross-sections of oxygen in the wavelength region 205-240 nm of the Herzberg continuum, Planetary and Space Science, 36, 1469–1475, https://doi.org/10.1016/0032-0633(88)90012-8, 1988.

Yoshino, K., Esmond, J., Sun, Y., Parkinson, W., Ito, K., and Matsui, T.: Absorption cross section measurements of carbon dioxide in the wavelength region 118.7-175.5 nm and the temperature dependence, Journal of Quantitative Spectroscopy and Radiative Transfer, 55, 53–60, https://doi.org/10.1016/0022-4073(95)00135-2, 1996.

Young, G., Long, D., Fedo, C., and Nesbitt, H.: Paleoproterozoic Huronian basin: Product of a Wilson cycle punctuated by glaciations and a meteorite impact, Sedimentary Geology, 141, 233–254, https://doi.org/10.1016/S0037-0738(01)00076-8, 2001.

Yung, Y., MA, A., and Pinto, J.: Photochemistry of the atmosphere of Titan - Comparison between model and observations, The Astrophysical journal. Supplement series, 55, 465–506, https://doi.org/10.1086/190963, 1984.

Zabarnick, S., Fleming, J., and Lin, M.: Kinetic study of the reaction $CH(X^2\prod)+H2 \rightleftharpoons CH2(X^3B_1)+H$ in the temperature range 372 to 675 K, Chemical Physics, 85, https://doi.org/10.1063/1.451808, 1986.

Zahnle, K.: Photochemistry of methane and the formation of Hydrocyanic Acid (HCN) in Earth's early atmosphere, Journal of Geophysical Research, 91, https://doi.org/10.1029/JD091iD02p02819, 1986.

Zahnle, K. and Walker, J. C.: A constant daylength during the Precambrian era?, Precambrian Research, 37, 95–105, 1987.

Zahnle, K., Claire, M., and DC, C.: The loss of mass-independent fractionation of sulfur due to a Paleoproterozoic collapse of atmospheric methane, Geobiology, 4, 271 – 283, https://doi.org/10.1111/j.1472-4669.2006.00085.x, 2006.